ACS NANO

www.acsnano.org

Article

Glyco-Cloaking Unlocks Cationic Aggregation-Induced Emission Luminogens for Myogenesis Support and On-Demand Photodynamic Antibacterial Action

Zeyan Zhuang, Yiwen Liao, Yu-Chien Lin, Jianqing Li, Han Ding, Jiayi Hu, Huajun Zhang, Zujin Zhao, Ben Zhong Tang, Hongwei Duan, Nam-Joon Cho, and Xue-Wei Liu*

Cite This: *ACS Nano* 2026, 20, 16876−16893

Read Online

ACCESS | Metrics & More | Article Recommendations | Supporting Information

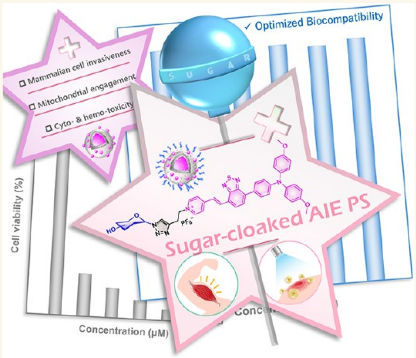

ABSTRACT: Antimicrobial resistance threatens both human health and economic stability, urgently demanding antibiotic-free infection strategies. This global crisis brings to the fore a central challenge in antimicrobial material design lying in reconciling potency with biocompatibility, a dilemma acutely epitomized by cationic amphiphilic materials, despite their longstanding therapeutic significance. To address this, we present a glyco-cloaked charge-masking strategy that converts an intrinsically toxic cationic scaffold into a biocompatible and multifunctional platform. By employing a deep-red aggregation-induced emission-active pyridinium scaffold, systematic glycosylation affords eight derivatives in acetyl-protected and deprotected forms. Glycosylation attenuates cationic charge exposure on nanoaggregates, dramatically reducing mammalian cell internalization, cytotoxicity, and hemolysis, while fully preserving robust photodynamic activity with efficient dual-type reactive oxygen species generation, alongside bacterial-targeting capability. Strikingly, the lead compound Man-PEBT enables precise intracellular bacterial imaging and on-demand photodynamic bacterial elimination *in vitro* and *in vivo*, concurrently demonstrating negligible myoblast toxicity and exceptional myogenesis compatibility, which redefines the functional scope of cationic materials. This work unites infection control with tissue support in a single platform and establishes glyco-cloaking as a transformative design strategy to bridge the critical efficacy−biocompatibility divide, offering a step toward a more sustainable bioeconomy and safer biomedicine.

KEYWORDS: *cationic amphiphile, aggregation-induced emission, photodynamic therapy, myogenesis, biocompatibility*

INTRODUCTION

The escalating global threat of antimicrobial resistance necessitates the development of innovative nonantibiotic strategies to effectively combat pathogenic infections in clinical settings and to mitigate microbial contamination across diverse industrial fields.[1,2] Cationic amphiphilic materials represent promising antimicrobial candidates[3−8] with a lower risk of mutation-driven resistance development[9,10] by disrupting bacterial envelopes through electrostatic and lipophilic interactions. However, their inherent toxicity toward mammalian cells, which induces membrane destabilization, mitochondrial dysfunction, and apoptotic signaling,[11−13] severely limits their practical applications. This not only raises safety concerns due to potential adverse outcomes but also undermines product quality and process reliability in industrial fields such as cellular agriculture and tissue engineering.[14−16]

To circumvent this inherent cytotoxicity while boosting antimicrobial efficiency, photodynamic therapy (PDT) has emerged as a compelling antimicrobial approach, driving the molecular design of cationic amphiphilic photosensitizers (PSs).[17−20] In PDT, light activation triggers the localized production of cytotoxic reactive oxygen species (ROS) from ambient oxygen, enabling reduced drug exposure and minimized off-target damage.[21,22] Notably, aggregation-induced emission-active PSs (AIE-PSs) have rapidly evolved as particularly promising candidates.[23−25] Unlike conventional PSs, which suffer from aggregation-caused fluorescence quenching and ROS suppression, AIE-PSs retain or even enhance their photophysical and bioactive functions in the aggregated state.[26,27] Yet, the cytotoxicity inherent to their cationic nature persists, underscoring the critical challenge of decoupling potent antimicrobial action from mammalian cell toxicity.[28−32]

Beyond merely mitigating adverse effects, achieving genuine biocompatibility in cationic amphiphilic systems opens new

Received: February 21, 2026
Revised: May 27, 2026
Accepted: May 28, 2026
Published: June 4, 2026

https://doi.org/10.1021/acsnano.6c03351

Scheme 1. Conception and Implementation of a Glyco-Cloaking Strategy[a]

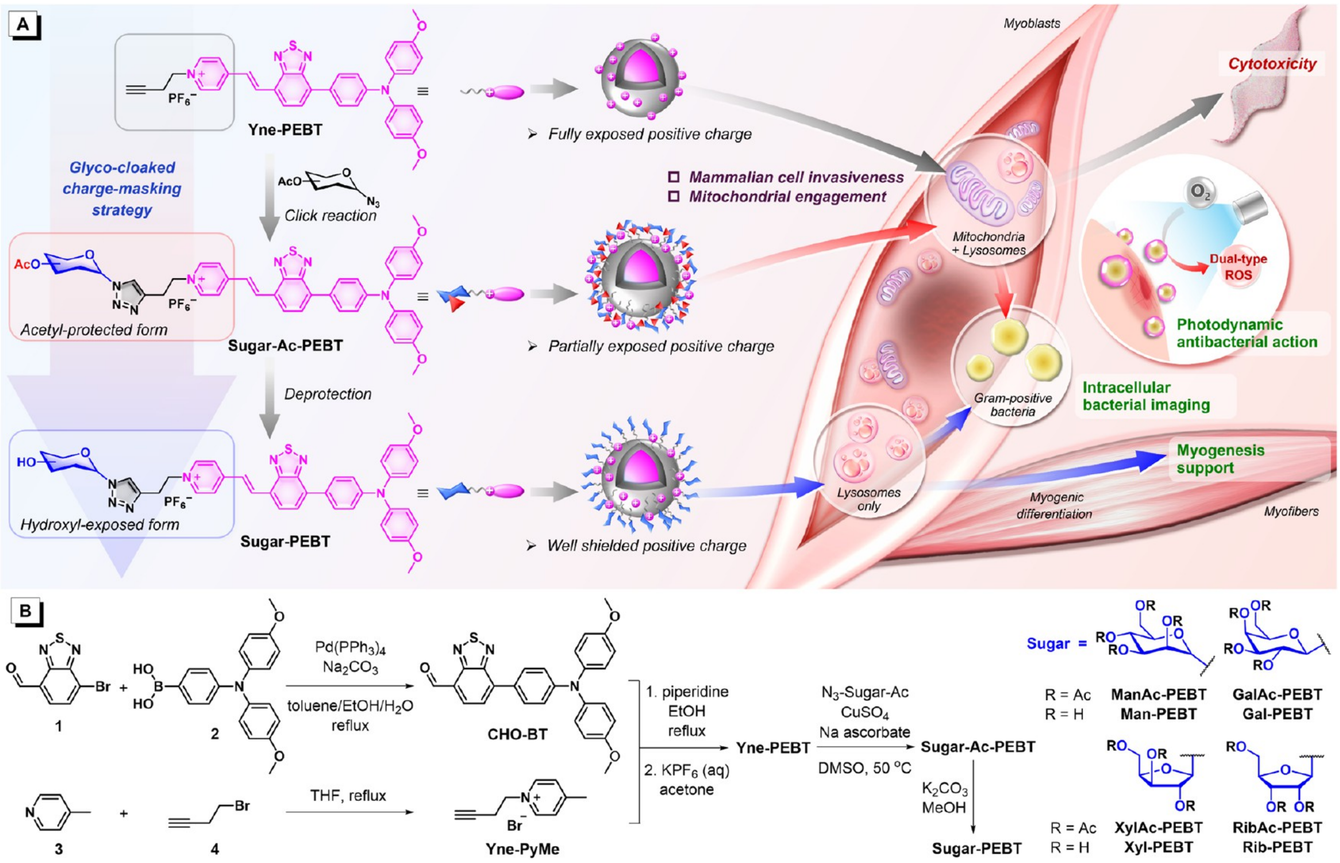

[a](A) Schematic illustration of the glyco-cloaked charge-masking strategy to optimize the biocompatibility of PEBT-based AIE-PSs, supporting myogenesis compatibility and enabling intracellular bacterial imaging and on-demand photodynamic antibacterial action. (B) Synthetic routes of Yne-PEBT and the glyco-cloaked PEBT derivatives.

opportunities to reveal benign material−cell interactions and to leverage inherent bioactivity to guide cellular processes.[33,34] This advancement paves the way for next-generation multifunctional antimicrobial materials.[35−40] Myogenesis, a finely orchestrated progression from myoblast differentiation to the formation of contractile myofibers,[41,42] serves as an ideal model demanding such a bifunctional platform. This process is exquisitely responsive to inductive environmental cues yet critically vulnerable to both microbial contamination and cytotoxic disruption. Beyond its physiological importance, controlled myogenesis is foundational to transformative biotechnologies, such as engineering functional tissue grafts and producing structured cultured meat.[43−45] Therefore, a platform that seamlessly integrates contamination prevention with myogenesis compatibility offers an economically sustainable solution for high-value applications, directly addressing pressing challenges in regenerative medicine and cellular agriculture.

Inspired by the widely adopted glycosylation approach in medicinal chemistry to precisely modulate physicochemical and pharmacological properties, including solubility, stability, and targeting specificity,[46−49] herein, we design a glyco-cloaked charge-masking strategy based on a pyridinium-containing AIE-PS platform. As depicted in Scheme 1A, an AIE-PS scaffold, denoted as Yne-PEBT, is designed based on a conjugated system composed of dimethoxytriphenylamine (MeOTPA), benzothiadiazole (BT), and vinylpyridinium (EPy) with a terminal alkyne.[50−52] It functions as both a synthetic precursor and a reference control for comparative studies while inherently enabling efficient dual-type (type I and type II) ROS generation upon light irradiation. A monosaccharide moiety, introduced in acetyl-protected or deprotected form, is anticipated to not only mask the surface positive charge of the pyridinium units, thereby attenuating electrostatic interactions, but also reduce hydrophobic associations with phospholipid membranes, collectively lowering cellular uptake and cytotoxicity.[53−55] Thereinto, the acetyl-protected variants, named Sugar-Ac-PEBTs, are designed to retain hydrophobic character and thus probe their role in biological interactions. In contrast, the deprotected counterparts with exposed hydroxyl groups, named Sugar-PEBTs, maximize hydrophilicity and optimal multivalent hydrogen bonding, which is also expected to contribute to enhanced bacterial binding strength via carbohydrate-mediated molecular recognition.[56,57] Through stepwise glycoengineering from Yne-PEBT to Sugar-Ac-PEBTs and finally to Sugar-PEBTs, we aim to optimize biocompatibility while fully preserving robust photodynamic activity with dual-type ROS generation and bacterial-targeting capability, offering a functional platform capable of on-demand antibacterial action with favorable myogenesis compatibility.

https://doi.org/10.1021/acsnano.6c03351
ACS Nano 2026, 20, 16876−16893

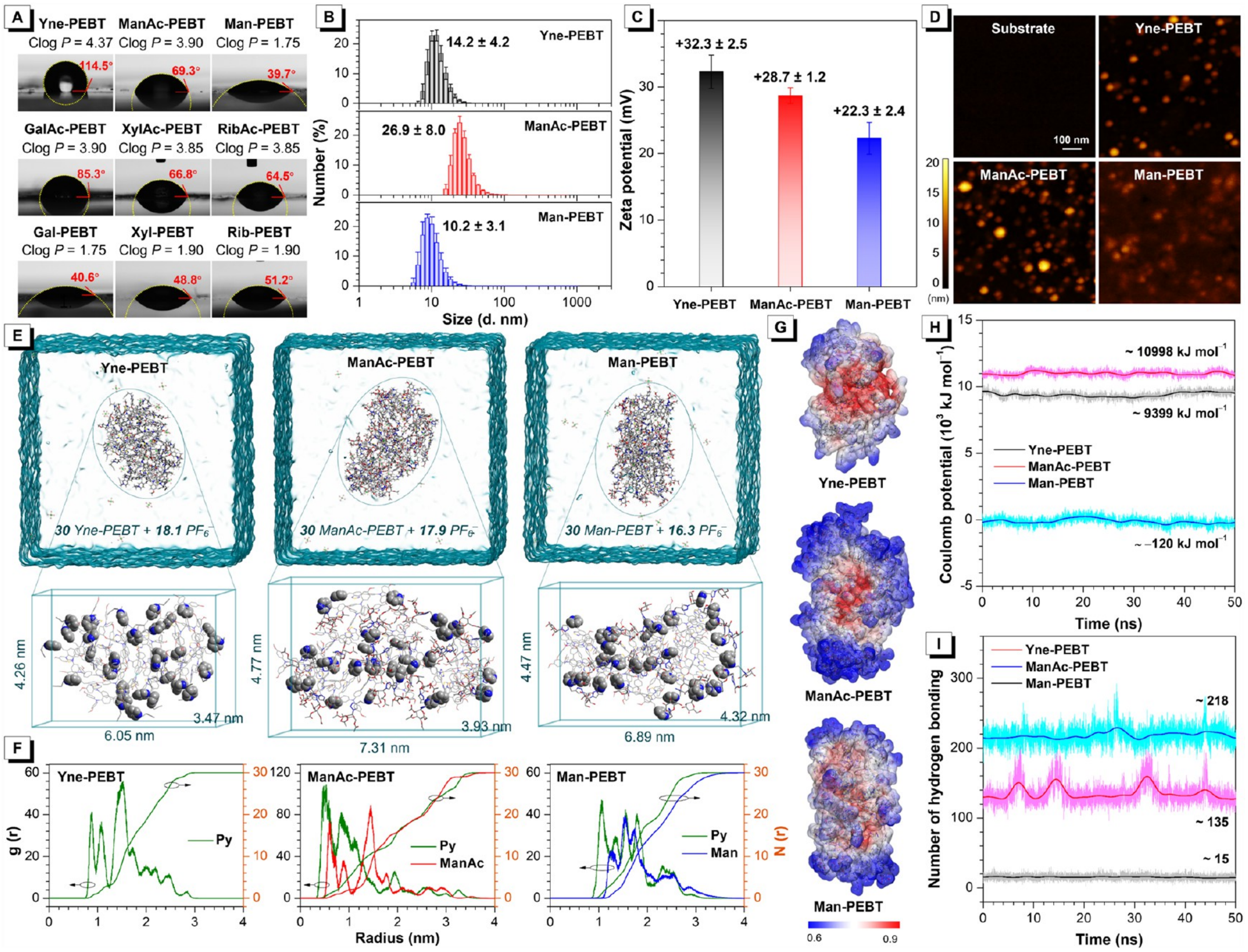

Figure 1. Physicochemical characterization and MD simulations. (A) Clog *P* values and water contact angles of Yne-PEBT and the glyco-cloaked PEBT derivatives. (B) Particle size distributions, (C) ζ-potentials, and (D) AFM images of Yne-PEBT, ManAc-PEBT, and Man-PEBT in water with 1 vol % dimethyl sulfoxide (DMSO). (E) MD simulation snapshots of aggregates formed by Yne-PEBT, ManAc-PEBT, and Man-PEBT with PF_6^- counterions in water. Enlarged views: molecular packing of PEBT aggregates shown without counterions, with the overall sizes annotated in virtual boxes. Pyridiniums are rendered as space-filling spheres, substituents attached to the pyridinium are displayed in tube, and the remaining parts are rendered in wireframe. (F) Radial distribution functions (RDF, g (r)) and accumulated numbers (N (r)) of pyridinium and sugar moieties within PEBT aggregates. (G) ESP mapping of Yne-PEBT, ManAc-PEBT, and Man-PEBT aggregates shown without counterions. Calculated (H) Coulomb potential of PEBT aggregates and (I) hydrogen bond numbers between PEBT aggregates and water (counterions excluded), with mean values derived from the shown data set.

RESULTS AND DISCUSSION

Synthesis and Characterization

The synthesis of Yne-PEBT and the modular construction of glyco-cloaked PEBT variants were outlined in Scheme 1B. The dialdehyde intermediate CHO-BT was synthesized via a Suzuki reaction between a brominated BT derivative (**1**) and a boronic acid-substituted MeOTPA moiety (**2**), coupling MeOTPA and BT units. Separately, the propargylated pyridinium salt, Yne-PyMe, was prepared by the alkylation of 4-methylpyridine (**3**) with 4-bromobut-1-yne (**4**). Knoevenagel condensation of CHO-BT with Yne-PyMe, followed by anion exchange with KPF_6, yielded the alkyne-functionalized AIE-PS, Yne-PEBT. In addition, a series of azido-functionalized acetylated monosaccharides (N_3−Sugar-Acs), involving two hexoses (mannose and galactose) and two pentoses (xylose in its furanose form and ribose), were prepared via azidation of their corresponding peracetylated precursors using trimethylsilyl azide ($TMSN_3$)/$SnCl_4$, following previously reported procedures (Scheme S1).[58−62] The terminal alkyne of Yne-PEBT was then conjugated to N_3−Sugar-Acs via copper-catalyzed azide−alkyne cycloaddition (CuAAC) click reaction, affording Sugar-Ac-PEBTs. Subsequent base-mediated deacetylation removed the acetyl-protecting groups, yielding the deprotected Sugar-PEBTs. This modular strategy facilitates the introduction of diverse sugar moieties, including mannose, galactose, xylose, and ribose, generating a library of glycosylated AIE-PSs. All products were characterized by nuclear magnetic resonance (NMR) spectroscopy, with final compounds further confirmed by high-resolution mass spectrometry (HRMS) (see ESI for details). Notably, a large coupling constant of ∼16 Hz is consistently observed between two vinyl protons for all the PEBT derivatives, unequivocally indicating the *trans* (*E*) configuration across the double bond.

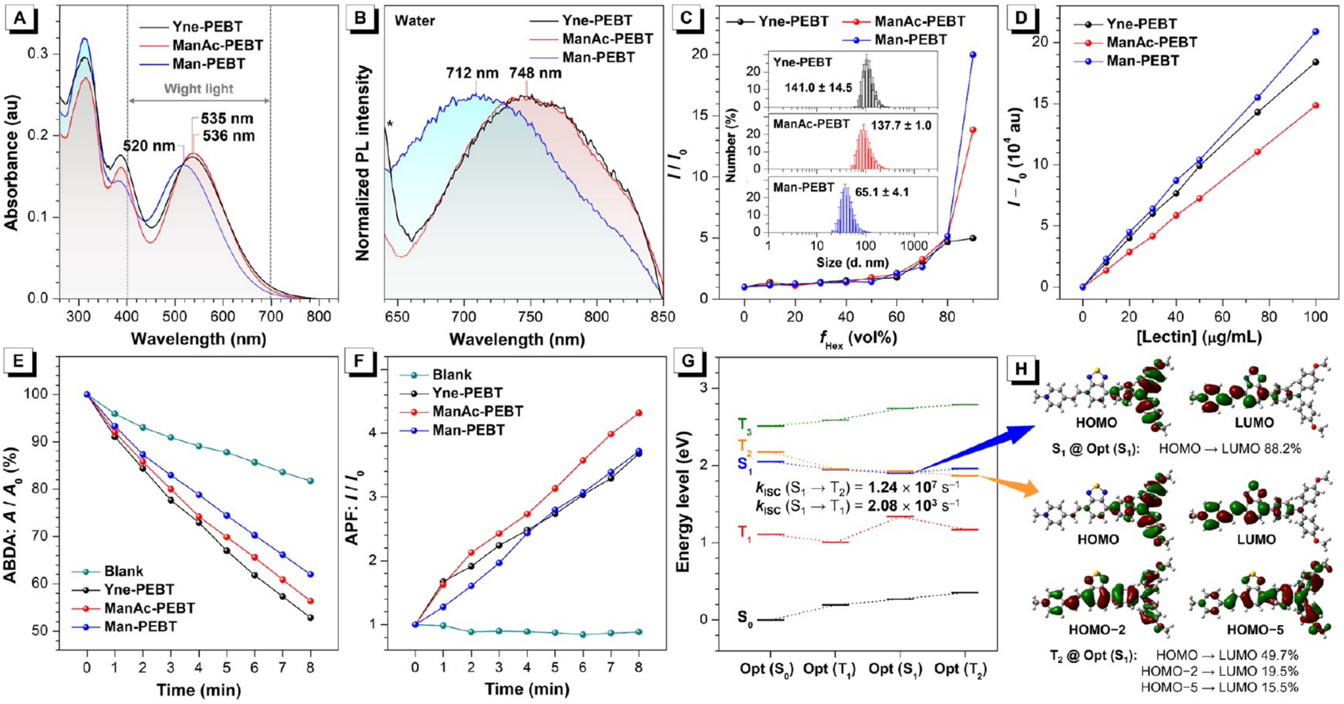

Figure 2. Photophysical properties and ROS-generating ability. (A) Absorption spectra of Yne-PEBT, ManAc-PEBT, and Man-PEBT in water with 1 vol % DMSO. Photoluminescence (PL) spectra of Yne-PEBT (Ex: 520 nm), ManAc-PEBT (Ex: 520 nm), and Man-PEBT (Ex: 500 nm) (B) in water with 1 vol % DMSO, where the asterisk denotes the Raman peak from solvent. (C) Plots of I/I_0 vs f_{Hex} of Yne-PEBT, ManAc-PEBT, and Man-PEBT in acetone/Hex mixtures, where I_0 is the PL intensity at $f_{\mathrm{Hex}} = 0$. Inset: Particle size distributions of Man-PEBT in Hex with 10 vol % acetone. (D) Fluorescence response ($I - I_0$) of Yne-PEBT, ManAc-PEBT, and Man-PEBT as a function of lectin concentration. (E) Plots of decomposition rates of ABDA for $^1O_2$ detection and (F) relative PL intensity of APF for OH$^\bullet$ detection in the presence of Yne-PEBT, ManAc-PEBT, or Man-PEBT in water with 1 vol % DMSO vs irradiation time. White light: 20 mW cm^{-2}. (G) Calculated energy diagram and (H) transition analysis of Me-PEBT with the dominating frontier molecular orbitals. HOMO = the highest occupied molecular orbital. LUMO = the lowest unoccupied molecular orbital. Concentration: 10 μM. The asterisk denotes the Raman peak from solvent.

Glyco-Cloaking Modulates Self-Assembly Behaviors and Aggregate Structures

Amphiphilicity was evaluated via calculated octanol/water partition coefficients (Clog *P*) and water contact angle measurements (Figure 1A). The parent compound, Yne-PEBT, which features a bulky hydrophobic segment with a cationic tail, exhibits pronounced hydrophobicity, as reflected by its high log *P* value and large water contact angle. Introducing acetylated sugar moieties (Sugar-Ac-PEBTs) moderately enhanced hydrophilicity, lowering both the log *P* and water contact angles. And this hydrophilic character was further amplified upon deacetylation (Sugar-PEBTs). Notably, hexose conjugates are less hydrophilic than pentose conjugates in their acetylated forms but become more hydrophilic postdeacetylation, a pattern consistent with the number of acetyl or hydroxyl groups present. These results confirm that our glycoengineering strategy successfully and systematically introduces a well-defined hydrophilicity gradient into the PEBT scaffold, ranging from the hydrophobic Yne-PEBT to the moderately hydrophilic Sugar-Ac-PEBTs and finally to the highly hydrophilic Sugar-PEBTs, with additional fine-tuning achieved through variations in sugar identity.

The aqueous self-assembly traits were then characterized by dynamic light scattering (DLS), which measured the particle sizes (Figures 1B, S1 and S2) and ζ-potentials (Figures 1C and S3). Yne-PEBT forms small, well-dispersed nanoaggregates with a highly positive ζ-potential, suggesting its electrostatic stabilization due to its fully exposed positive charges. Sugar-Ac-PEBTs tend to form larger aggregates with slightly lower ζ-potentials, indicating enhanced hydrophobic association and attenuated electrostatic repulsion. In contrast, Sugar-PEBTs yield the smallest nanoparticles with further reduced ζ-potentials, likely attributed to the hydroxyl-rich sugar corona, which forms effective hydration shells that shield the underlying cationic charges and provide colloid stabilization. These nanoaggregates exhibit well-defined size distributions with only modest size reduction upon dilution, without evident disassembly (Figure S2). Atomic force microscopy (AFM) of representative compounds (Yne-PEBT, ManAc-PEBT, and Man-PEBT) was then performed to visualize the aggregate morphology (Figure 1D). While Yne-PEBT and ManAc-PEBT form discrete particles with sharp edges, Man-PEBT presents poorly defined aggregates with diffuse boundaries, supporting the presence of hydration interactions.

To gain molecular-level insights, molecular dynamics (MD) simulations were performed for Yne-PEBT, ManAc-PEBT, and Man-PEBT, each comprising 30 molecules with 30 hexafluorophosphate (PF_6^-) counterions in water. All three systems form a single dominant coassembly cluster incorporating all 30 cations and a subset of counterions, with the remaining anions dispersed in bulk water (Figures 1E and S4). Enlarged views illustrate a general packing trend where hydrophobic π-conjugated backbones adopt compact packing in the interior, while hydrophilic pyridiniums and the linked substituents orient toward the surface, leading to the exposure of positive charges that are electrostatically compensated by associated PF_6^-. The spatial distributions of pyridiniums were then analyzed to elucidate their surface charge organization. In the

Yne-PEBT aggregate, pyridiniums are prominently localized at the periphery (Figure 1F), yielding high solvent-accessible surface areas (SASAs) for both the pyridiniums and the nitrogen atoms (Figure S5). This configuration drives maximal PF_6^- association (Figure S4), a pronounced positive electrostatic potential (ESP, Figure 1G), and a high Coulombic potential (Figure 1H), indicative of the maximized charge exposure. The ManAc-PEBT aggregate also exhibits a preference for peripheral pyridiniums with a fraction of ManAc groups folding inward, creating a more dispersed distribution of pyridiniums and a disordered arrangement of ManAc groups. Thus, its pyridinium SASAs remain high, requiring large PF_6^- association and producing a heterogeneous ESP with relatively high Coulombic energy. In stark contrast, Man-PEBT aggregates featured a distinctive intermediate pyridinium distribution, with an outer mannose layer that functions as an effective charge-shielding barrier. This yields the lowest pyridinium SASAs and PF_6^- association, a uniformly attenuated ESP, and a near-neutral Coulombic potential. This result largely arises from the extensive hydrogen-bonding network established by the free hydroxyl groups (Figure 1I). These MD simulations corroborate experimental observations, strongly supporting that the deprotected sugar moieties on Sugar-PEBT expose their hydroxyl groups in the aqueous environment, thereby effectively masking the surface positive charges of the nanoaggregates.

Glyco-Cloaking Retains Photophysical Properties and Dual-Type ROS-Generating Ability

The photophysical properties of the PEBT derivatives were characterized to assess the impact of glyco-cloaking. In water, all compounds exhibit broad absorption across the visible region (400−700 nm) centered in the green region (Figures 2A and S6) and broad spanning the emission in the red-to-near-infrared (NIR) region (640−850 nm), peaking above 700 nm with minimal concentration-dependent shifts (Figures 2B and S7). This profile supports efficient white-light harvesting for PDT and background-free fluorescence for bioimaging. Notably, Sugar-PEBTs show blue-shifted absorption and emission peaks compared to Yne-PEBT and Sugar-Ac-PEBTs, which are ascribed to distinct molecular packing modes within aggregates. The hydrophobic interactions in Yne-PEBT and Sugar-Ac-PEBTs promote ordered stacking and a polar internal environment that causes bathochromic shifts, while the hydration-driven assembly of Sugar-PEBTs disfavors ordered internal packing that minimizes bathochromic shifts. The AIE characteristics were then evaluated in two solvent systems: DMSO/water mixtures to induce aggregation in polar media (Figures S8−S11) and acetone/hexane (Hex) mixtures for nonpolar environments (Figures S11 and S12). Upon the addition of water to DMSO solutions, all compounds exhibit emergent red-to-NIR fluorescence from the PEBT core, and similarly, progressively enhanced red emission is observed upon hexane addition to acetone solutions. These results collectively confirm the AIE behavior of Yne-PEBT and its glyco-cloaked derivatives, wherein aggregation restricts intramolecular motions of the PEBT core, suppresses nonradiative decay, and thereby activates fluorescence. Notably, their emissions in nonpolar environments are blue-shifted relative to those in aqueous aggregates, reflecting environmental polarity effects and highlighting their potential as polarity-sensitive fluorescent indicators.

Given the AIE attributes, we investigated the fluorescence responses of the PEBT derivatives upon interaction with lectin (Figure S13), a representative carbohydrate-binding protein found on bacterial surfaces.[56,57] As shown in Figure 2D, the PEBT derivatives show linear fluorescence enhancement upon lectin-mediated recruitment, indicative of their comparable electrostatic attraction toward this negatively charged protein. Notably, relative to Yne-PEBT, Man-PEBT displays stronger responses, whereas ManAc-PEBT shows a significantly attenuated response, supporting the existence of carbohydrate−lectin interactions as an attraction that compensates for the charge-shielding effect imposed by the sugar moieties.

The ROS generation capabilities of all the PEBT derivatives in aqueous aggregates were evaluated under white-light irradiation. Considering the two ROS generation routes,[63,64] 9,10-anthracenediyl-bis(methylene)dimalonic acid (ABDA)[65] and aminophenyl fluorescein (APF)[66] were employed as specific indicators for singlet oxygen ($^1O_2$, type II ROS) and hydroxyl radicals ($OH^\bullet$, type I ROS), respectively. Upon irradiation, continuous degradation of ABDA (Figures 2E and S14) and progressive APF fluorescence enhancement (Figures 2F and S15) are observed for all compounds (Figure S16), demonstrating significant dual-type ROS generation capacity. In addition, the ability of Man-PEBT, as an example, to generate superoxide anion radicals ($O_2^{\bullet-}$, type I ROS) is verified by electron paramagnetic resonance (EPR) spectroscopy using 5,5-dimethyl-1-pyrroline *N*-oxide (DMPO) as a spin trap (Figure S17). Notably, the incorporation of sugar results in a slight but variable reduction in ROS generation efficiency compared to the parent Yne-PEBT, with the specific sugar architecture exerting a significant influence. Sugar-PEBTs consistently exhibit lower ROS yields than their corresponding acetylated counterparts, due to their less compact aggregate structures, which may facilitate nonradiative decay pathways at the expense of ROS production. Moreover, hexose-based conjugates (both acetylated and deacetylated) generally produce higher ROS levels than those based on pentose, suggesting that greater steric bulk is beneficial to ROS output. Despite this attenuation, the glyco-cloaked PEBT derivatives retain substantial dual-type ROS production, supporting their applicability as effective PSs in aqueous environments.[67,68]

To decipher the ROS generation mechanism of the PEBT core, theoretical calculations were performed on the model Me-PEBT, where the bulky substituent on pyridinium was replaced with a methyl. An energy-level diagram (Figure 2G) was constructed based on optimized ground (S_0), first excited singlet (S_1), and low-lying triplet (T_1 and T_2) state geometries. The results reveal that direct intersystem crossing (ISC) from S_1 to T_1 is inefficient, with a low ISC rate constant (k_{ISC}). A highly efficient ISC channel exists between S_1 and T_2, enabled by a small adiabatic energy gap (ΔE) and a substantially elevated k_{ISC}. The two states share nearly identical electronic configurations with holes on MeOTPA and electrons on the BT−EPy segment, revealing strong charge-transfer (CT) character, which rationalizes the efficient ISC. Following the T_2 population, rapid internal conversion would funnel the system into the T_1 state, which acts as a long-lived reservoir for subsequent interaction with oxygen. The adiabatic energy gap between S_0 and T_1 is ~1.00 eV, meeting the thermodynamic threshold for $^1O_2$ generation (>0.98 eV), thereby validating the feasibility of the type II ROS pathway. In parallel, the singly occupied molecular orbital (SOMO) localization on the BT−EPy segments (Figure S18) together with a large electron

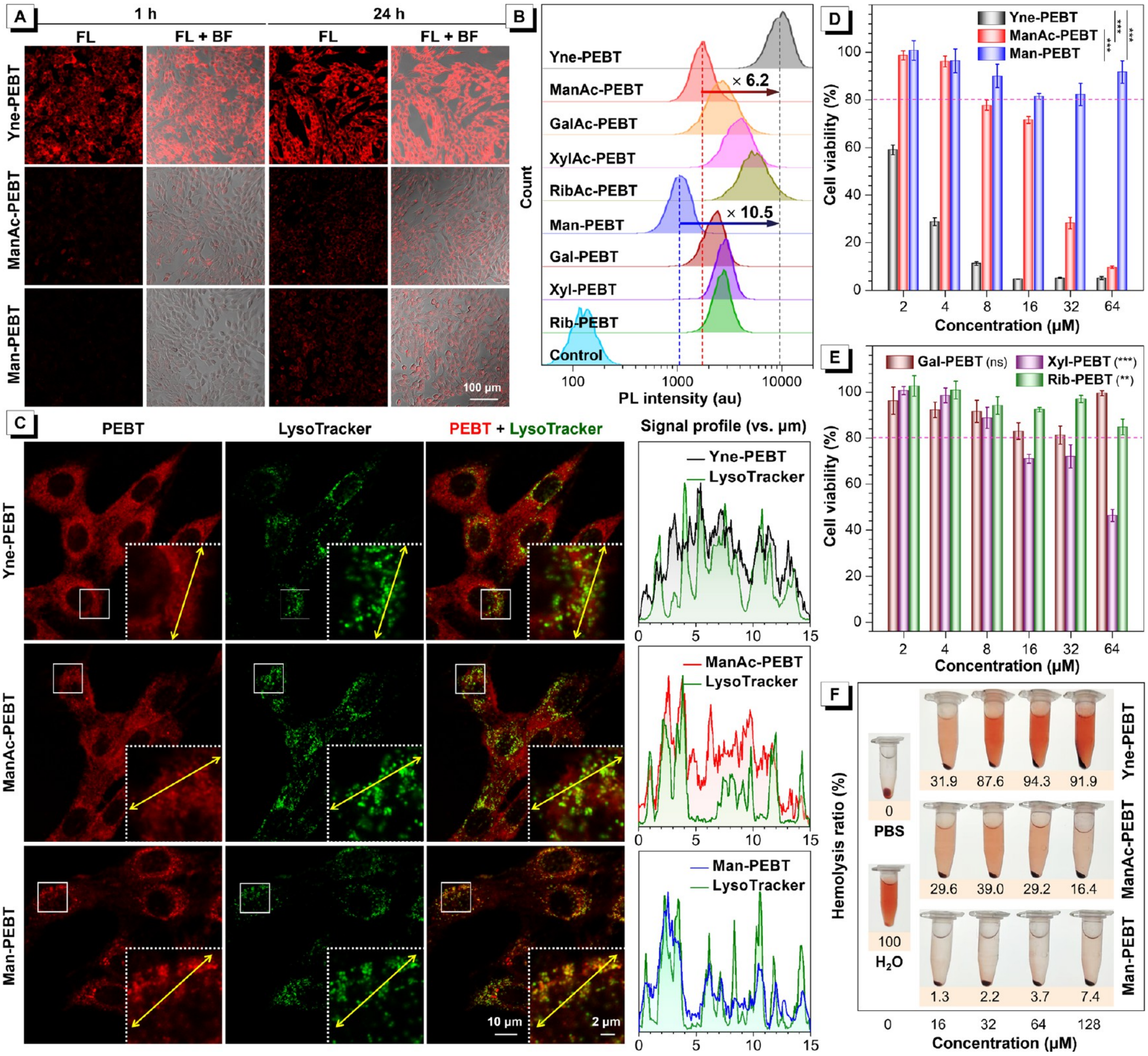

Figure 3. Mammalian cellular internalization and biocompatibility. (A) Fluorescent images of C2C12 cells stained by Yne-PEBT, ManAc-PEBT, or Man-PEBT in growth medium (4 μM). Ex = 561 nm, Em = 570−740 nm. (B) Flow cytometry of C2C12 cells stained by Yne-PEBT or the glyco-cloaked PEBT derivatives in growth medium (4 μM, 1 h). Ex = 561 nm, Em = 710/50 nm. (C) Colocalization images of C2C12 cells costained by Yne-PEBT, ManAc-PEBT, or Man-PEBT (4 μM, 1 h) with Lyso-Tracker Green in growth medium, with the intensity profile of synchrony for the yellow line. (D) Cell viability of C2C12 after treatment with Yne-PEBT, ManAc-PEBT, or Man-PEBT in growth medium for 3 d. Magenta lines indicate the threshold of 80% cell viability. Data are presented as mean ± standard deviation (SD), $n = 3$, $***p < 0.001$. (E) Cell viability of C2C12 after treatment with Sugar-PEBT derivatives in growth medium for 3 d. Magenta lines indicate the threshold of 80% cell viability. Data are presented as mean ± SD, $n = 3$. ns = not significant, $**p < 0.01$, $***p < 0.001$ vs Man-PEBT in (D). (F) Hemolysis of red blood cells induced by different concentrations of Yne-PEBT, ManAc-PEBT, or Man-PEBT. FL = fluorescent channel. BF = bright field.

affinity from T_1 to the radical doublet state (−5.66 eV) confirms that the electron-deficient moiety can capture and stabilize an electron from exogenous reductants, pointing to a viable type I pathway. These theoretical findings are consistent with the experimentally observed dual-type ROS generation capacity of the PEBT core.

Glyco-Cloaking Reduces Cellular Internalization and Enables Biocompatibility

The cellular internalization of the PEBT derivatives was systematically assessed in C2C12 mouse myoblasts. Fluorescence imaging (Figures 3A and S19) reveals that Yne-PEBT is rapidly internalized by C2C12 cells, exhibiting strong cytoplasmic fluorescence within 1 h in growth, differentiation, and basic media. Prolonging incubation to 24 h further intensifies the signal, suggesting sustained accumulation. In contrast, all glyco-cloaked PEBT derivatives exhibit only faint intracellular signals under all conditions (Figure S20), indicating that the glyco-cloaking substantially impedes cellular internalization. This trend was corroborated in NIH/3T3 mouse fibroblasts (Figure S21). Leveraging their similar emission maxima (~700 nm, Figure S22), flow cytometry

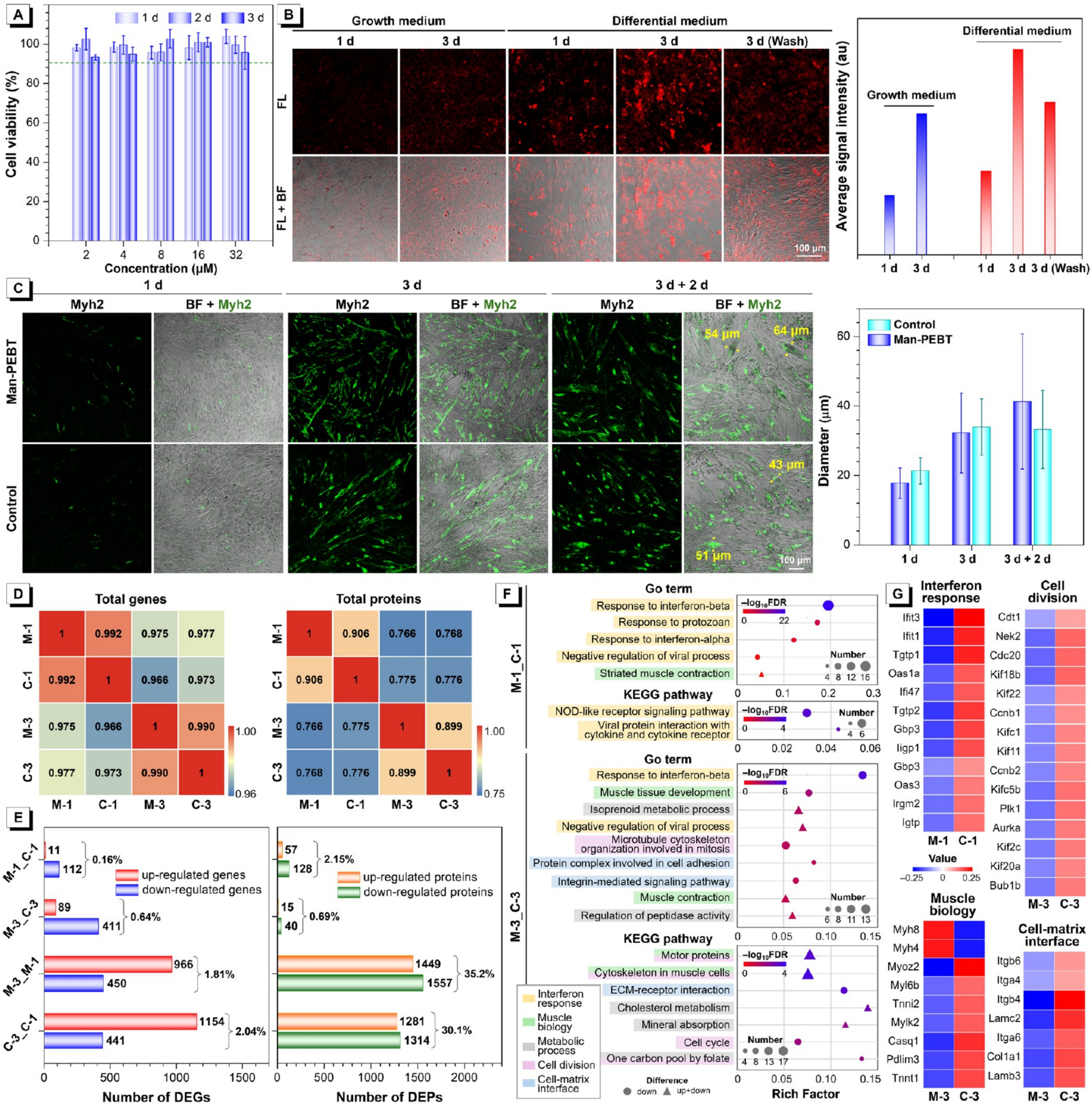

Figure 4. Myogenesis compatibility and regulation capacity. (A) Cell viability of C2C12 cells after treatment with Man-PEBT in various media. The green line indicates the threshold of 90% cell viability. Data are presented as mean ± SD, $n = 3$. (B) Fluorescent images of C2C12 cells stained by Man-PEBT in growth or differentiation medium for 1 or 3 d (4 μM), with the average signal intensity of the field of view. Ex = 561 nm, Em = 570−740 nm. (C) Myh2 immunofluorescence staining image of C2C12 cells with or without Man-PEBT (4 μM) in differentiation medium for 1, 3, and 3 d followed by 2 d incubation in fresh differentiation medium (3 d + 2 d), with the diameters of the two representative myotubes labeled in yellow and statistical analysis of myotube diameters from the field of view (Data are presented as mean ± SD, $n > 50$). (D) Correlation heatmaps of total gene and protein expression profiles from control and Man-PEBT groups at different differentiation stages (1 and 3 d), using Pearson correlation. (E) DEG and DEP counts between M-1_C-1, M-3_C-3, M-3_M-1, and C-3_C-1 comparisons. (F) Enriched GO BP terms and KEGG pathways for M-1_C-1 and M-3_C-3 comparisons. (G) Cluster heatmap of representative DEGs related to interferon response (M-1_C-1), cell division (M-3_C-3), cell-matrix interface (M-3_C-3), and muscle biology (M-3_C-3) processes regulated by Man-PEBT. GO = Gene Ontology. KEGG = Kyoto Encyclopedia of Genes and Genomes.

was further employed to quantify the cellular uptake efficiency, which shows a consistent rank order of Yne-PEBT ≫ Sugar-Ac-PEBTs > Sugar-PEBTs (Figures 3B and S23). Striking differences emerge as early as 1 h of incubation, where ManAc-PEBT and Man-PEBT display the lowest signals with mean intensities 6.2-fold and 10.5-fold lower than that of Yne-PEBT, respectively. This points to mannose-based moieties as particularly effective kinetic barriers to cellular entry, likely owing to their superior hydrophilicity and greater steric bulk relative to other sugars tested.

The environmental influences on cellular internalization were then clarified. Uptake of all Yne-PEBT, ManAc-PEBT, and Man-PEBT is markedly suppressed at 4 °C relative to 37 °C (Figure S24), confirming that energy-dependent endocytosis serves as the predominant entry pathway. Lowering serum content strongly enhanced uptake, most pronounced for Yne-PEBT, probably due to the adsorption of the cationic amphiphiles onto serum proteins. ManAc-PEBT and Man-PEBT show relatively reduced serum dependence, reflecting greater resistance to protein interference, owing to the charge shielding by glyco-cloaking. Critically, the uptake of ManAc-PEBT and Man-PEBT remains largely unaffected by various free monosaccharides (Figure S25), indicating that the internalization bypasses specific sugar receptors on mammalian cells, in contrast to Yne-PEBT inhibited by free sugars. Together, these results demonstrate that glyco-cloaking confers enhanced stability against nonspecific protein and sugar interference in complex biological environments, enabling more predictable and controlled cellular outcomes than the highly efficient but less selective parent Yne-PEBT.

To further elucidate the subcellular distribution, costaining assays were performed using commercial organelle-specific markers. All Yne-PEBT, ManAc-PEBT, and Man-PEBT show pronounced colocalization with LysoTracker Green (Figure 3C), indicating their enrichment within lysosomes, consistent with endocytic uptake, although additional distributions in other regions exist to varying extents. Strikingly, Yne-PEBT also exhibits significant mitochondrial colocalization (Figure S26), likely driven by electrostatic attraction to the mitochondrial membrane potential. This mitochondrial engagement is progressively attenuated in ManAc-PEBT and nearly absent in Man-PEBT, aligning with the charge-shielding effect of the glyco-cloaking, which potentially contributes to lowered cytotoxicity and enhanced biosafety.

The cytotoxicity of the PEBT derivatives was assessed in C2C12 myoblasts, NIH/3T3 fibroblasts, and HaCaT human keratinocytes in growth medium using the 3-(4,5-dimethylthiazol-2-yl)-2,5-diphenyltetrazolium bromide (MTT) assay (Figures 3D, E and S27−S29). Yne-PEBT exhibits pronounced, concentration- and time-dependent toxicity in all cell lines, consistent with its efficient cellular accumulation and mitochondrial engagement. In contrast, Sugar-Ac-PEBTs exhibit moderate toxicity across all cell lines, whereas Sugar-PEBTs maintain high cell viability throughout, confirming that glyco-cloaking effectively attenuates the intrinsic toxicity of the PEBT core. Impressively, Man-PEBT outperforms other Sugar-PEBTs, preserving >90% viability after 1 day and >80% after 3 days across all tested concentrations (2−64 μM), which aligns with its minimal cellular uptake. Collectively, Sugar-PEBTs demonstrate broad mammalian safety, with mannose emerging as the optimal shielding group that confers the highest biocompatibility among all sugars evaluated.

Hemolysis assays were further performed on Yne-PEBT, ManAc-PEBT, and Man-PEBT (Figure 3F). Yne-PEBT exhibits severe, concentration-dependent hemolytic activity, while ManAc-PEBT induces moderate hemolysis. Man-PEBT, however, exhibited greatly enhanced hemocompatibility, maintaining <5% hemolysis up to 64 μM. These findings align with the cytotoxicity profiles, collectively underscoring that glyco-cloaking successfully decouples the intrinsic toxicity of the PEBT core.

Man-PEBT Shows Myogenesis Compatibility and Regulation Potential

Having established the cytocompatibility of Man-PEBT under standard conditions, its long-term effects in the more physiologically complex and stringent context of myogenic differentiation were evaluated. This process is highly sensitive to microenvironmental stress, making it a rigorous benchmark for assessing biomaterial compatibility beyond short-term cell survival.[69,70] Under differentiation-inducing conditions, Man-PEBT maintains >90% cell viability across 2−32 μM over 3 d (Figure 4A), confirming its robust safety profile during this critical transition. While most other derivatives (except Gal-PEBT) exhibit markedly elevated cytotoxicity in differentiation media (Figures S30 and S31), consistently more pronounced than under standard growth conditions, underscoring the heightened vulnerability of cells undergoing differentiation. Fluorescence images reveal that glyco-cloaked PEBT derivatives exhibit a progressive accumulation in the extracellular space, a signal largely eliminated by washing, while a stable intracellular component persists (Figures 4B, S32, and S33), suggesting they preferentially associate with the newly deposited extracellular matrix (ECM),[71,72] rather than being stably internalized by cells, during differentiation induction. Myogenic differentiation was then evaluated by myosin heavy chain 2 (Myh2, a mature myotube marker)[73,74] immunofluorescence and morphological observation (Figure 4C), revealing roughly comparable progression between control and Man-PEBT-treated groups. At day 1, faint Myh2 signals and aligned myocytes mark early commitment. By day 3, Myh2 expression surges, with the appearance of elongated multinucleated myotubes. Following the 3 d + 2 d regimen (treatment followed by 2 d in Man-PEBT-free medium), robust myofibers form with overall comparable diameter distributions.[75,76] Notably, Man-PEBT-treated groups exhibit some thicker myofibers at later stages, with representative fibers reaching diameters up to ∼108 μm (Figure S34), suggesting a positive regulatory influence on myofiber maturation, potentially mediated through ECM interactions that modulate the differentiation microenvironment.[77,78]

To elucidate the molecular basis of Man-PEBT compatibility with myogenesis, transcriptomic and proteomic analyses were performed on C2C12 cells at differentiation day 1 (initiation phase, Man-PEBT-1 d, M-1; Control-1 d, C-1) and day 3 (active fusion phase, Man-PEBT-3 d, M-3; Control-3 d, C-3). Multivariate analysis of total gene and protein expression profiles reveals that the primary driver of molecular variation stems from normal differentiation progression, with clear separation between 1-d and 3-d samples (Figures 4D and S35).[79] With gene expression and protein synthesis remaining largely unaltered, Man-PEBT induces slight molecular perturbations (Figures 4E and S36−S38). Differentially expressed genes (DEGs) account for only 0.16% and 0.64% of genes for M-1_C-1 and M-3_C-3, respectively, of transcripts, versus ∼2% during normal differentiation transitions. Differentially expressed proteins (DEPs) comprise only 2.15% and 0.69%, for M-1_C-1 and M-3_C-3, respectively, of the proteome, whereas stage transitions engage >30%. These results confirm that Man-PEBT exerts only limited and subtle molecular perturbations without disrupting the overarching architecture of myogenic differentiation.

Functional enrichment analysis was then performed based on the transcriptomic data (Figure 4G and F), as no significantly enriched pathways were identified from the

https://doi.org/10.1021/acsnano.6c03351
ACS Nano 2026, 20, 16876−16893

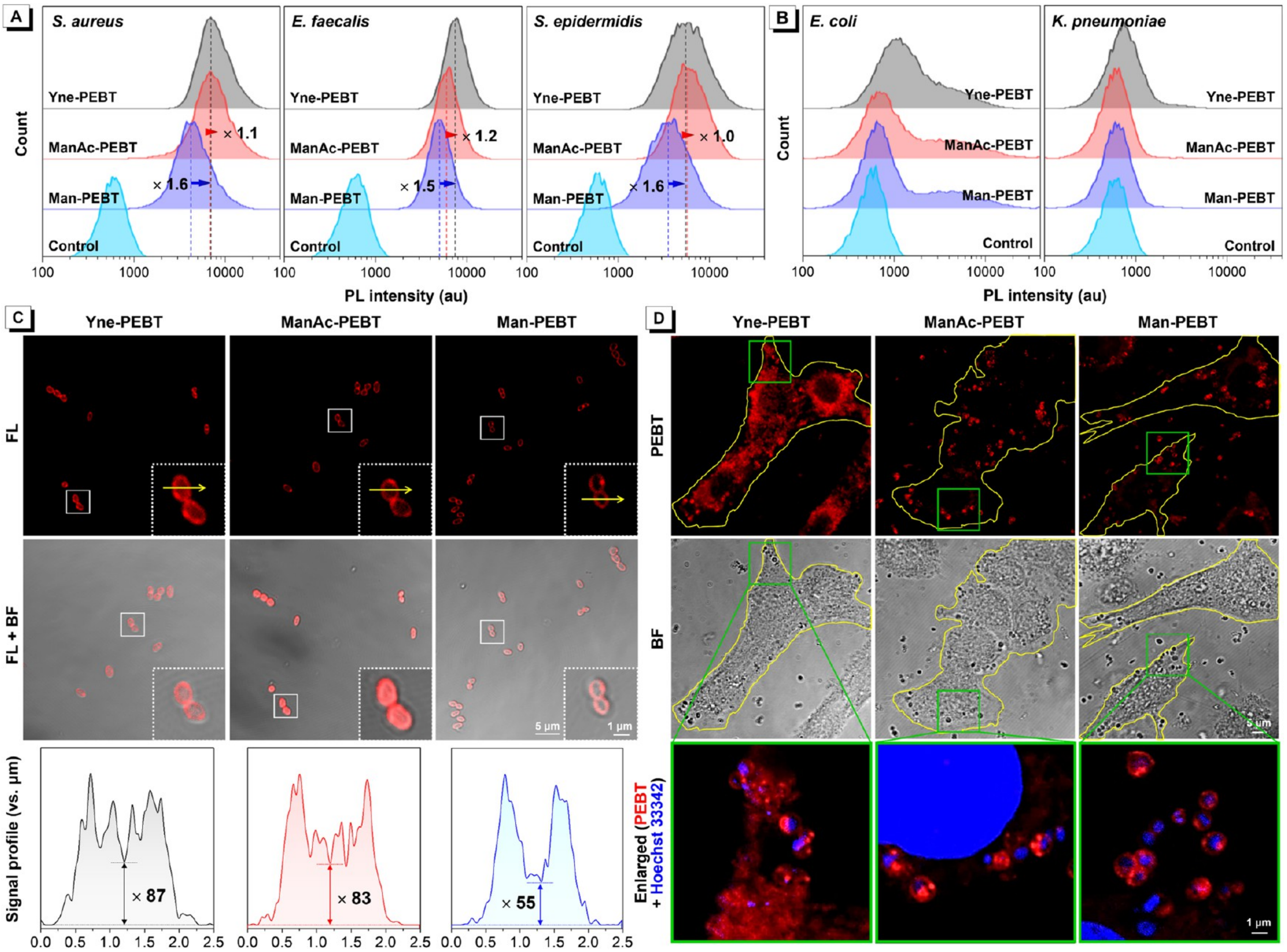

Figure 5. Bacterial staining and intracellular bacterial imaging. Flow cytometry of various (A) Gram-positive and (B) Gram-negative bacteria stained by Yne-PEBT, ManAc-PEBT, or Man-PEBT (4 μM, 30 min). (C) Fluorescent images of *E. faecalis* stained by Yne-PEBT, ManAc-PEBT, or Man-PEBT (4 μM, 30 min), with enlarged images of the white dashed square and the intensity profile of synchrony for the yellow line. (D) Fluorescent images of *S. aureus*-infected C2C12 cells stained by Yne-PEBT, ManAc-PEBT, or Man-PEBT (4 μM, 30 min) in basic media, with enlarged regions in the green square.

proteomic data set, likely due to the inherent limitations of protein coverage and detection sensitivity in mass spectrometry. At day 1 (M-1_C-1), Man-PEBT downregulated interferon-related pathways, moderating inflammatory activation to foster a balanced environment conducive to differentiation initiation.[80] Striated muscle contraction pathways are also enriched, featuring upregulation of *Myh8* alongside downregulation of *Chrnd*, *Mylk2*, and *Cxcr4*, which suggests a specific and nuanced influence of Man-PEBT on the developing contractile apparatus.[81] From day 1 to day 3 (M-3_M-1, C-3_C-1), a pronounced shift from proliferation toward muscle differentiation occurs[82] (Figure S39). By day 3 (M-3_C-3), enriched pathways cluster into several key biological categories. Cell division pathways are characterized by the coordinated downregulation of a core set of mitotic genes compared with standard differentiation, suggesting that Man-PEBT may contribute to safeguarding the differentiation process by limiting excessive proliferation. Concurrently, interferon signaling remains downregulated, consistent with day 1 patterns, resolving transient inflammation to create a permissive niche for later myogenesis. In addition, pathways governing the cell-matrix interface show coordinated downregulation of integrins, laminins, and collagens, implying microenvironmental remodeling that may reduce adhesion constraints and favor myoblast fusion, providing a molecular context for the enhanced fusion phenotype observed.[83,84] Complementing these changes, muscle biology pathways reveal marked upregulation of terminal effector genes *Myh8* (embryonic/developmental fast-twitch) and *Myh4* (mature fast-twitch), suggesting a transitional state toward specialized fast-twitch programming and offering a rationale for localized myotube hypertrophy.[85,86]

Collectively, these multiomics findings demonstrate that Man-PEBT achieves high myogenic compatibility through remarkably subtle molecular perturbations, while coordinately modulating the inflammatory, proliferative, and adhesive microenvironment to guide orderly differentiation toward a defined fast-twitch phenotype. This establishes a robust molecular foundation for the application of Man-PEBT in skeletal muscle engineering.

Glyco-Cloaking Improves Bacterial Staining and Achieves Intracellular Bacterial Imaging

To assess the bacterial staining efficacy of these PEBT derivatives, flow cytometric analysis was performed on a panel of representative bacterial strains, including Gram-

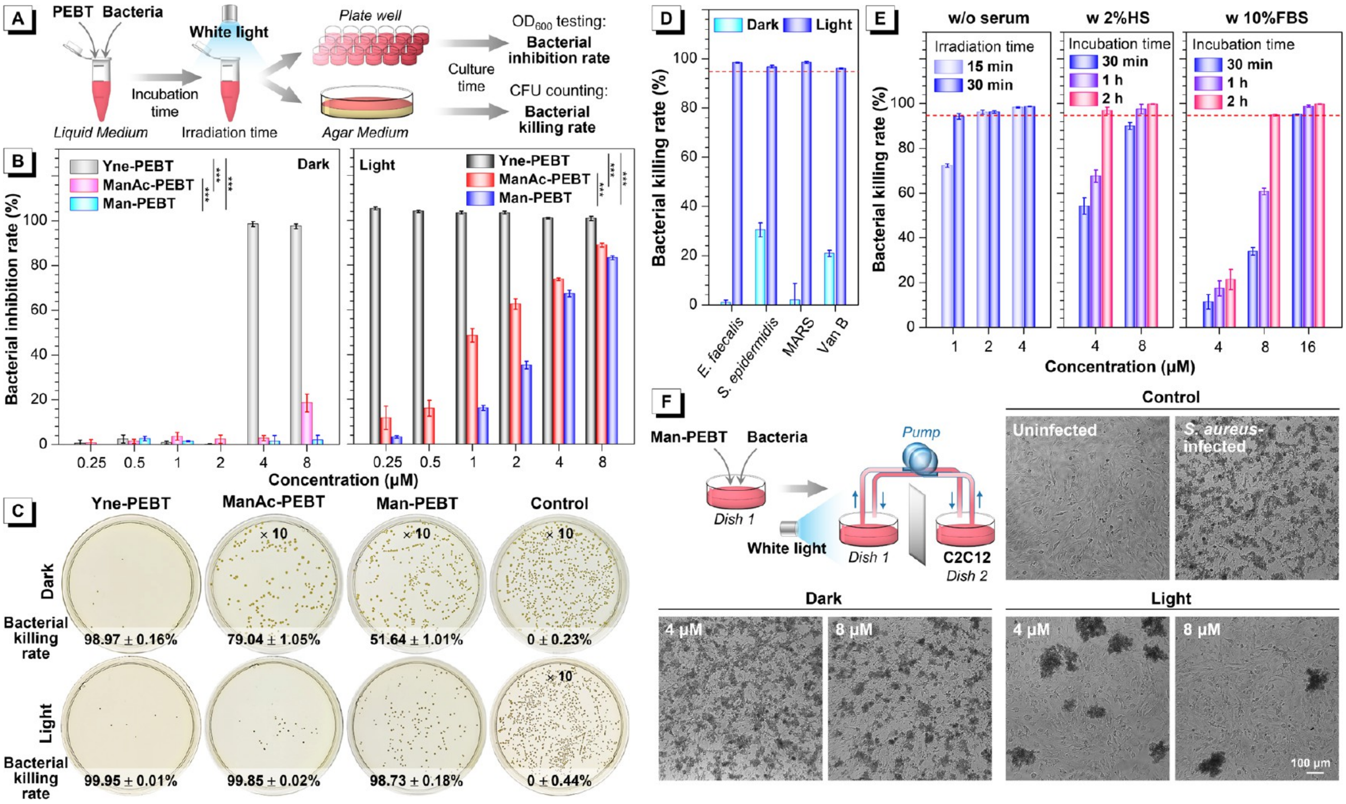

Figure 6. On-demand photodynamic antibacterial action. (A) Schematic illustration of bacterial inhibition and killing rate assay. (B) Bacterial inhibition rates of Yne-PEBT, ManAc-PEBT, and Man-PEBT (30 min before irradiation) toward *S. aureus* in LB without or with irradiation at varied concentrations. (C) Representative CFU photos of *S. aureus* after being treated with Yne-PEBT, ManAc-PEBT, or Man-PEBT (4 μM, 30 min, in DMEM) without or with irradiation, with bacterial killing rates. (D) Bacterial killing rates of Man-PEBT (4 μM, 30 min before irradiation, in DMEM) toward various bacteria without or with irradiation. Red lines indicate the threshold of 95% bacterial killing rates. (E) Bacterial killing rate of Man-PEBT (30 min before irradiation if not indicated, in DMEM without or with serum) toward *S. aureus* with irradiation at varied conditions. Red lines indicate the threshold of 95% bacterial killing rates. (F) Schematic illustration of the fluidic coculture system for localized irradiation and BF images of *S. aureus*-infected C2C12 cells treated with Man-PEBT in differentiation medium without or with irradiation. Flow rate: 0.2 mL min^{-1}. HS = horse serum. FBS = fetal bovine serum. White light: 20 mW cm^{-2}, 30 min if not indicated. Data are presented as mean ± SD, $n = 3$, $^{***}p < 0.001$.

positive species of *S. aureus*, *E. faecalis*, and *S. epidermidis*, and Gram-negative species of *E. coli* and *K. pneumoniae*. Yne-PEBT, ManAc-PEBT, and Man-PEBT produce substantial fluorescence signals across all tested Gram-positive strains (Figure 5A). In contrast, markedly weaker fluorescence is observed in Gram-negative bacteria (Figure 5B), underscoring a pronounced binding preference of PEBT derivatives for Gram-positive strains. This preference arises from anionic teichoic acids on Gram-positive surfaces that attract cationic amphiphiles, versus the lipopolysaccharide barrier in Gram-negatives.[87,88] Notably, Yne-PEBT and ManAc-PEBT show comparable intensities in Gram-positive strains, both ~1.5–1.8-fold higher than Man-PEBT. This modest difference contrasts sharply with the pronounced uptake disparity observed in mammalian cells, indicating that glycosylation preferentially reduces mammalian affinity while largely preserving bacterial association. All glyco-cloaked PEBT derivatives consistently exhibit robust staining efficacy in Gram-positive bacteria (Figure S40), reinforcing the universal staining efficacy. While Yne-PEBT, ManAc-PEBT, and Man-PEBT stained *S. aureus* consistently in basic media like Luria–Bertani (LB) and plain Dulbecco's Modified Eagle Medium (DMEM), serum addition elicits divergent responses (Figure S41). Yne-PEBT remains largely unchanged, reflecting strong electrostatic binding with bacteria resistant to protein competition. ManAc-PEBT shows a gradual signal decline with increasing serum concentration, while Man-PEBT exhibits the most pronounced reduction, with the signals remaining considerable. This prompted us to verify their performance in subsequent antibacterial assays under serum-containing conditions. Free monosaccharide supplementation leads to an unexpected fluorescence enhancement for Yne-PEBT (Figure S42), likely reflecting strengthened binding associated with metabolic modulation in the bacterial membrane potential induced by the added carbon source. Conversely, ManAc-PEBT and Man-PEBT exhibit largely unchanged fluorescence upon sugar addition, indicating that their preinstalled sugar moieties already provide interactions comparable to free monosaccharides, which are not readily displaced, likely owing to concurrent electrostatic interactions. These results support that electrostatic attraction remains the dominant force for bacterial association, while carbohydrate-mediated interactions provide an auxiliary contribution.[56,57]

Fluorescence imaging was performed on *E. faecalis* to further investigate the subcellular localization. All Yne-PEBT, ManAc-PEBT, and Man-PEBT exhibit deep red fluorescence centered ~700 nm (Figure S43), clearly outlining the bacterial morphology (Figure 5C). Costaining with Hoechst 33342, a DNA-specific dye, confirms negligible cytoplasmic overlap (Figure S44), supporting envelope-specific localization. In-

https://doi.org/10.1021/acsnano.6c03351

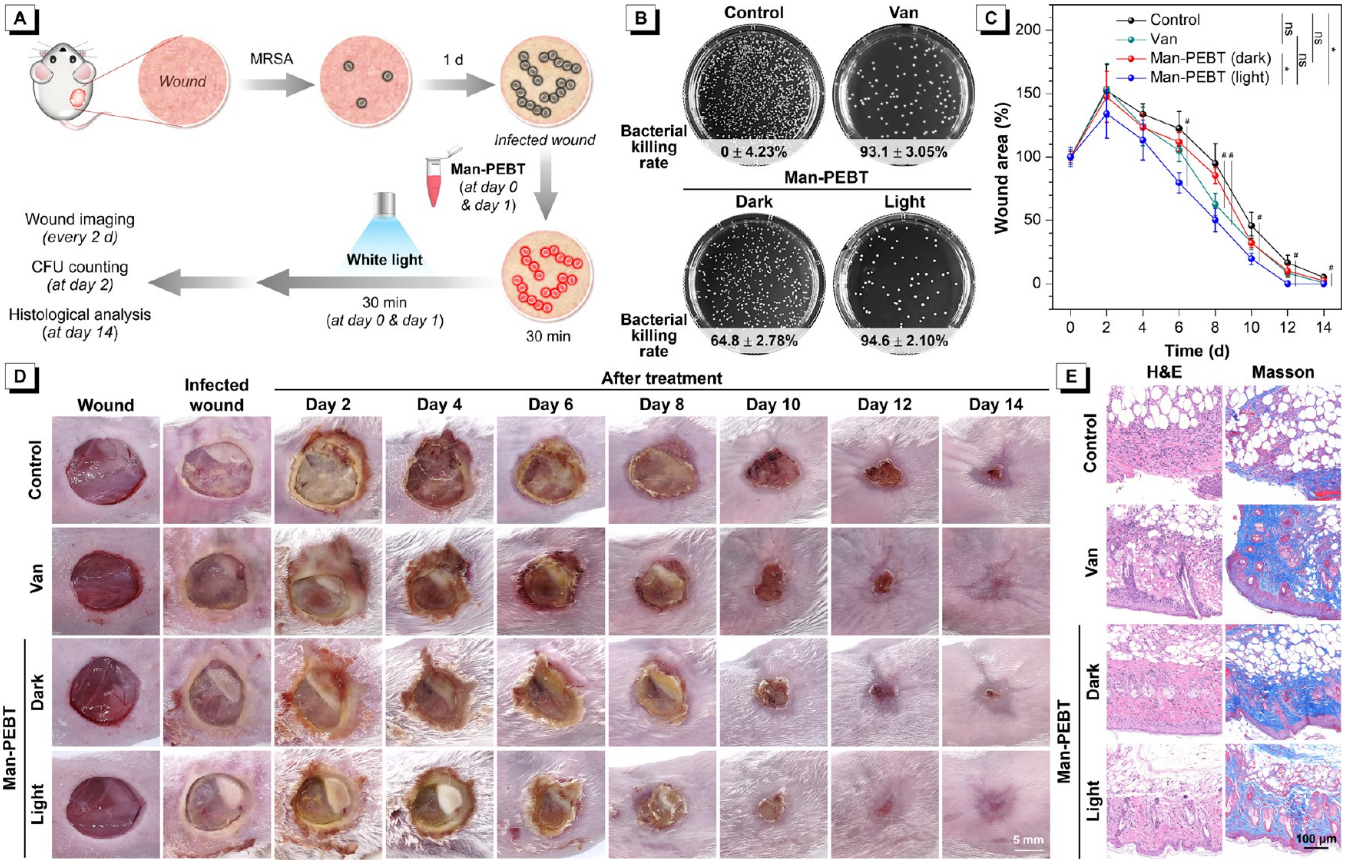

Figure 7. (A) Schematic illustration of the establishment and treatment of the MRSA-infected wound model. (B) Representative CFU photos of MRSA with bacterial killing rates. (C) Quantitative wound area analysis and (D) representative photos of wounds during the healing process. Data are presented as mean ± SD, $n = 3$. ns = not significant, $^{*}p < 0.05$, $^{\#}p < 0.05$. (E) H&E and Masson's trichrome staining images of wound tissues.

tensity profiles across individual cells exhibit dual peripheral peaks corresponding to the envelope regions, separated by a central valley representing the cytoplasm (Figures 5C and S45). Yne-PEBT and ManAc-PEBT show moderate cytoplasmic signals, indicating partial internalization beyond envelope binding. In contrast, Man-PEBT produces the weakest cytoplasmic fluorescence with the most clearly defined cell outline and the sharpest envelope peaks, achieving superior envelope confinement with minimal intracellular leakage, potentially limiting unintended interactions with genetic substrates and mitigating resistance risk.

In a physiologically relevant coculture model of *S. aureus*-infected C2C12 myoblasts in both basic (Figure 5D) and differentiation (Figure S46) media, Yne-PEBT displays diffuse and nonspecific distribution throughout the mammalian cytoplasm with poorly resolved bacterial outlines, rendering Yne-PEBT incompetent for intracellular bacteria labeling in host−pathogen coculture systems. This limitation likely stems from its efficient host-cell uptake and organelle accumulation, which produce substantial background interference. In sharp contrast, both ManAc-PEBT and Man-PEBT generate bright and well-defined signals that clearly delineate intracellular *S. aureus* with low background interference. This enhanced selectivity stems from their superior affinity for Gram-positive bacteria, coupled with low interaction with mammalian components, enabling precise visual detection of pathogens within host environments for infection monitoring.

Glyco-Cloaking Achieves On-Demand Photodynamic Antibacterial Action

The antibacterial efficacy of the PEBT derivatives was evaluated by measuring the bacterial inhibition rates, which were gauged by optical density (OD_{600}) after treatment and incubation (Figure 6A). Without light, Yne-PEBT exhibits substantial inhibitory activity against *S. aureus* (Figure 6B) and *E. faecalis* (Figure S47), with a minimum inhibitory concentration (MIC) of 4 μM. In contrast, ManAc-PEBT and Man-PEBT show negligible inhibition across 0.25−8 μM, indicating that glycol-cloaking effectively dissociates bacterial staining capability from the inherent toxicity of the PEBT core. Upon irradiation, all three compounds exhibit a markedly enhanced inhibitory activity, with Yne-PEBT showing the highest potency, resulting from the synergy of dark toxicity and photodynamic activity. Meanwhile, ManAc-PEBT and Man-PEBT exhibit strongly concentration-dependent inhibition, reaching rates exceeding 80% at 8 μM, confirming that photodynamic action dominates without appreciable background toxicity. This light-activated inhibition is consistent across other glyco-cloaked PEBT derivatives (Figure S48). Although the overall inhibition rate is compromised relative to Yne-PEBT, these light-activated behaviors offer better spatiotemporal control capability, thereby achieving on-demand PDT. Importantly, none of Yne-PEBT, ManAc-PEBT, and Man-PEBT inhibits the growth of Gram-negative *E. coli*, either in dark or light conditions (Figure S49), which is consistent with their limited staining effect toward Gram-negative strains as observed.

https://doi.org/10.1021/acsnano.6c03351
ACS Nano 2026, 20, 16876−16893

We next quantified the bacterial killing rates via colony-forming unit (CFU) counting after treatment (Figure 6A). Yne-PEBT achieves >90% killing rates as low as 0.125 μM, which is further enhanced to >99% eradication upon irradiation even at 0.031 μM (Figure S50). While potently synergistic, its pronounced dark activity limits spatiotemporal selectivity for photodynamic applications. In contrast, ManAc-PEBT and Man-PEBT show inadequate killing in the dark but achieve >99% and >98% eradication, respectively, upon irradiation, confirming their reliance on photodynamic action. This light-activated killing efficacy extends across multiple strains, including nonresistant strains of *E. faecalis* and *S. epidermidis* and drug-resistant pathogens of methicillin-resistant *S. aureus* (MRSA) and vancomycin-resistant *E. faecalis* (Van B) (Figures 6D and S51−S53). In all cases, Yne-PEBT shows a similarly thorough bactericidal effect, while glyco-cloaked PEBT derivatives consistently achieve >96% photodynamic killing, confirming the broad-spectrum photodynamic efficacy. Given their serum susceptibility in bacterial binding, the antibacterial potency of ManAc-PEBT and Man-PEBT against *S. aureus* is verified with the presence of serum (Figures 6E and S54−S57), which shows partially compromised, particularly for Man-PEBT. This serum-induced reduction is largely attributable to the formation of protein coronas. Nevertheless, ManAc-PEBT and Man-PEBT retain potent killing activity when adequate concentrations, incubation time, or irradiation doses are applied, owing to the dynamic and reversible nature of the protein corona, which does not act as a permanent barrier.

Given these results, we further evaluated Man-PEBT in a fluidic host−pathogen coculture model under differentiation conditions, where the intermediate serum level provides a feasible context for Man-PEBT to exert antibacterial activity (Figure 6F). In this system, uninfected C2C12 cells form a confluent monolayer, whereas *S. aureus* infection produces dense bacterial colonies that disrupt the cellular layer. Man-PEBT fails to control *S. aureus* proliferation without irradiation. Upon continuous illumination, 4 μM Man-PEBT significantly mitigates *S. aureus* colonization, and 8 μM Man-PEBT achieves improved bacterial clearance, leaving only sparse residual microcolonies while fully preserving the C2C12 monolayer. This demonstrates the feasibility of Man-PEBT for contamination management in complex biological settings, and further optimization of flow dynamics and light delivery potentially enhances outcomes.

Following wound creation, bacterial inoculation, and purulence formation, Man-PEBT was administered with or without subsequent white light irradiation, alongside vancomycin (Van) as a positive control. As shown in Figure 7B, Man-PEBT reduces bacterial load upon irradiation with a high bacterial killing rate reaching 94.6%, comparable to that of Van (93.1%), whereas Man-PEBT in the dark achieves a moderate reduction of 64.8%. This result demonstrates that Man-PEBT achieves potent *in vivo* photodynamic antibacterial action on par with a clinically used antibiotic. Wound healing was monitored every 2 days (Figure 7C and D). Although all groups initially exhibit slight wound expansion accompanied by purulence and inflammation, these symptoms are markedly alleviated in the Man-PEBT (light) groups. From day 6 onward, the Man-PEBT (light) group exhibits significantly accelerated wound contraction compared to the control and Man-PEBT (dark) groups. Although the overall healing trend of the Man-PEBT (light) group is statistically comparable to that of the Van group, it demonstrates a more pronounced improvement relative to the control at multiple time points. The Man-PEBT (light) group achieves near-complete closure by day 12, while the Van group shows delayed closure with complete healing observed only by day 14, and the control and Man-PEBT (dark) groups retain visible scabs even at day 14. Histological analysis at day 14 further supports these observations (Figure 7E). Both the Van and Man-PEBT (light) groups show well-restored tissue architecture, including continuous epidermis and organized collagen deposition. Notably, the Man-PEBT (light) group displays a more pronounced collagen alignment and clearer tissue organization, indicative of effective remodeling. In comparison, the control group shows a disrupted epidermis and significant inflammatory infiltration, while the Man-PEBT (dark) group exhibits only partial recovery with residual inflammation. These results highlight that Man-PEBT-mediated photodynamic antibacterial action not only achieves antibacterial efficacy comparable to Van but also promotes efficient wound healing, likely through simultaneous infection eradication and inflammation control. Furthermore, histological assessment of major organs harvested post-treatment shows no detectable tissue damage, inflammatory infiltration, or structural abnormalities in all groups (Figure S58). Consistently, longitudinal body weight monitoring throughout the experiment reveals no significant differences among groups (Figure S59), confirming the favorable *in vivo* biosafety profile of Man-PEBT.

CONCLUSION

In this study, we designed and implemented a glyco-cloaked charge-masking strategy based on the red-emissive AIE-PS scaffold PEBT, yielding a family of glyco-cloaked PEBT derivatives with inherent dual-type ROS generation capacity. The introduced sugar moieties finely tune molecular amphiphilicity and sterically mask the exposed cationic charges in their aqueous nanoaggregates, thereby reducing nonspecific association with biological membranes and lowering the level of uptake by mammalian cells. Consequently, both cytotoxicity and hemolysis associated with the inherent positive charge are markedly attenuated, signifying the successful transformation of the originally cytotoxic cationic core to a biocompatible platform with robust long-term biosafety. Importantly, all glyco-cloaked PEBT derivatives retain desired fluorescence and potent photodynamic activity against Gram-positive bacteria, while displaying abrogated dark toxicity relative to the parent Yne-PEBT, thereby enabling on-demand photodynamic antibacterial action.

Among the series, Man-PEBT stands out as an optimal candidate, exemplifying the success of this strategy. It exhibits negligible toxicity toward myoblasts and maintains high compatibility throughout myogenesis, as validated at the morphological, molecular, and pathway levels. Furthermore, initial observations suggest that Man-PEBT may subtly influence myogenic differentiation trajectories, likely through ECM-mediated interactions that may reduce adhesion constraints and favor myoblast fusion. Although the phenotypic effects in the present model are localized, they provide a rationale for future optimization of culture parameters (e.g., initial cell density, dosage regimen, and adhesion substrate) to potentially enhance the inductive regulatory capacity. Moreover, Man-PEBT enables intracellular bacterial detection via fluorescence imaging and exerts robust photodynamic antibacterial actions across multiple validation

https://doi.org/10.1021/acsnano.6c03351
ACS Nano 2026, 20, 16876−16893

models, from *in vitro* assays and host−pathogen coculture models to an *in vivo* wound infection model.

Overall, this study establishes glyco-cloaking as a transformative design strategy that redefines the functional scope of cationic materials, uniting infection control with tissue support in a single platform to bridge the critical efficacy−biocompatibility divide. The present Man-PEBT platform is ideally suited for *ex vivo* decontamination of transparent liquids and superficial, optically accessible infections, where its on-demand light-controlled antibacterial action offers distinct advantages over global or systemic treatment. Beyond these immediate applications, this work opens a path toward next-generation biomedical and bioengineering platforms with promising implications for regenerative medicine, cellular agriculture, and integrated theranostics, offering a step toward a more sustainable bioeconomy and safer biomedicine.

EXPERIMENTAL SECTION

Materials and Instruments

C2C12 mouse myoblast, NIH/3T3 mouse fibroblast, and HaCaT human keratinocyte cell lines, *S. aureus* (ATCC 29213), *E. faecalis* (ATCC 29212), *S. epidermidis* (ATCC 12228), MRSA (ATCC BAA38), Van B (ATCC 51299), *E. coli* (K12), and *K. Pneumoniae* (ATCC BAA-2784) were obtained from the American Type Culture Collection (ATCC) and handled according to the protocols. The 4-week-old female BALB/c mice were purchased from GemPharmatech. Ultrapure water was supplied by a Millipore Milli-Q Plus System. Other materials were purchased from commercial sources and used as received without further purification. NMR spectra were measured on a JEOL JNM-ECA 400SL spectrometer in deuterated solvents using tetramethylsilane (TMS; $\delta = 0$) as the internal reference at room temperature. Liquid chromatography−mass spectrometry (LC-MS) was conducted on a Thermo Fisher Scientific LTQ XL mass spectrometer. HRMS was conducted on a Waters Xevo G2-X2 high-resolution mass spectrometer. Static water contact angles were measured on a KRUSS DSA25 instrument via the sessile drop method (3-μL droplets, Young−Laplace fitting), for which thick films were prepared by drop-coating a methanol solution of the compound onto glass substrates, and measurements were repeated at least 3 times across different surface regions at ambient conditions. Particle size analysis and zeta potential measurement were performed on a Malvern Zetasizer Nano-ZSP. AFM images were obtained on a Bruker Dimension XR Icon system in PeakForce tapping mode with a tip of SCM-PIT-V2. UV−vis absorption spectra were measured on a Shimadzu UV-2300 spectrophotometer. PL spectra were recorded on a Horiba Fluoromax-4 fluorescence spectrophotometer. EPR measurements were carried out on a JEOL JES-X310 electron spin resonance spectrometer. Cell counting was conducted on a Bio-Rad TC20 automated cell counter. Microscopy images were obtained on a Zeiss LSM800 laser scanning confocal microscope, an LSM980 laser scanning confocal microscope (CLSM) with Airyscan2 microscopy, or an Invitrogen EVOS M5000 Imaging System. Flow cytometry was conducted by a Becton Dickinson Fortessa X20 flow cytometer. The cell viability or bacterial concentration analysis was conducted by using a PerkinElmer EnSpire multimode plate reader at a wavelength of 600 nm. The instruments used for transcriptome sequencing and proteome sequencing were provided by Shanghai Meibo Biopharmaceutical Biotechnology. Further details regarding the synthesis and characterization can be found in the ESI.

MD Simulations

Geometric structure optimization and frequency analysis were performed using the density functional theory (DFT) method with the ωB97XD hybrid functional at the basis set level of 6-31G(d,p) through the Gaussian 16 package, Revision B.01. No symmetry constraint was applied for optimization. These data were then used to generate topology files through Sobtop.[89] Force field parameters for the cationic PEBT derivatives were assigned based on Hessian-derived vibrational analysis in conjunction with the General Amber Force Field (GAFF), and force constants for the hexafluorophosphate anion (PF_6^-) were derived from Hessian calculations. Atomic partial charges were determined using the RESP2(0.5) scheme as implemented in Multiwfn 3.8.[90] MD simulations were performed with Gromacs 2020.3 using the Amber99SB force field. To acquire the aggregate models, 30 molecules of Yne-PEBT, ManAc-PEBT, or Man-PEBT and 30 PF_6^- molecules were randomly placed in a cubic simulation box. For Yne-PEBT, a cubic box of 10.7 × 10.7 × 10.7 nm was used, with 39598 TIP3P water molecules. For ManAc-PEBT, a cubic box of 11.6 × 11.6 × 11.6 nm was used, with 50543 TIP3P water molecules. For Man-PEBT, a cubic box of 11.0 × 11.0 × 11.0 nm was used, with 42729 TIP3P water molecules. Simulations were conducted under periodic boundary conditions (PBC) in all directions with a Verlet cutoff scheme of 1.2 nm for both van der Waals and short-range electrostatic interactions. Long-range electrostatics were handled using the Particle Mesh Ewald (PME) method with a Fourier spacing of 0.16 nm^{-1}. The Verlet integration scheme was applied with a time step of 2 fs, and trajectory data were saved every 20,000 steps. Each simulation exceeded 300 ns in total length, and the final 50 ns of the equilibrated trajectory were used for statistical analysis. Surface electrostatic potential (ESP) was calculated based on RESP2(0.5) charge using Multiwfn 3.8.[91]

Quantum Mechanics Calculations

Quantum mechanics calculations were performed using the Gaussian 16 package, Revision B.01. The ground-state and excited-state calculations of an isolated molecule were performed using the DFT and time-dependent DFT (TD-DFT) method, respectively, under the level of ωB97XD/6-31G(d,p). No symmetry constraint was applied for optimization. Intersystem crossing rate (k_{ISC}) values were calculated by MOMAP 2024A[92] based on TD-DFT results and spin−orbit coupling (SOC) values calculated by using ORCA 5.0.1[93] at the level of ωb97X-D3/def2-TZVP on the optimized S_1 geometries.

Cell Culture and Cellular Staining

C2C12 and NIH/3T3 cells were maintained in DMEM supplemented with 10% FBS and 1% penicillin-streptomycin in a humidified incubator at 37 °C under 5% CO_2. Cell passage was performed every 2−3 d using 0.25% trypsin. Cell culture media used for the study include 10% FBS-containing DMEM (growth medium), 2% HS-containing DMEM (differentiation medium), and serum-free DMEM (basic medium). Cells were seeded in 12-well plates or confocal dishes, and ∼80% confluence was reached for the experiment. For cellular staining, after incubation with medium containing specified concentrations of PEBT derivatives for defined durations, either at 37 or 4 °C, cells were directly imaged by CLSM or detached with trypsin for flow cytometry analysis. For colocalization assays, cells were incubated with PEBT derivatives, followed by replacement with medium containing 500 nM LysoTracker Green or MitoTracker Green for 30 min at 37 °C before CLSM imaging.

Cell Viability Assay

Cells were seeded in a 96-well plate at a density of $\sim 10^5$ cells/mL and incubated with varying concentrations of PEBT derivatives for defined durations at 37 °C. The medium was then replaced with fresh medium containing 0.5 mg/mL MTT and incubated for 4 h at 37 °C. After removing the MTT solution, DMSO was added to dissolve the formazan crystals. After gently shaking the plate for 3 min, the absorbance of each well was measured at 600 nm by a microplate reader. Pairwise significance markers are omitted for clarity, and comparisons are based on mean trends. A two-way analysis of variance (ANOVA) was performed with compound and concentration as factors, including their interaction, to compare the overall trends in cell viability between the two compound groups across the tested concentration series. ns = not significant, $*p < 0.05$, $**p < 0.01$, $***p < 0.001$.

Hemolytic Test

Red blood cells were isolated from 1 mL of fresh blood by centrifugation (2500 rpm, 5 min) and washed three times with saline. The RBC pellet was resuspended to a 10% (v/v) suspension in saline. Aliquots (0.2 mL) of this suspension were incubated for 2 h at 37 °C with 0.8 mL of PBS containing varying concentrations of PEBT derivatives. PBS alone and ultrapure water served as negative and positive controls, respectively. After centrifugation (2500 rpm, 5 min), 200 μL of supernatant from each sample was transferred to a 96-well plate, and absorbance at 545 nm was measured. The hemolysis percentage was calculated relative to the positive control.

Immunofluorescence Analysis

C2C12 cells were fixed in 4% paraformaldehyde (PFA) for 15 min at room temperature and then permeabilized using 0.5% Triton X-100 for 15 min at room temperature. After blocking with 5% BSA for 30 min at room temperature, the cells were incubated with Myosin-2/Myh2 antibody (A4.74)-Alexa Fluor 488 conjugate for 1 h at 37 °C (1:100 dilution). Then, the cells were washed and imaged by CLSM.

Transcriptomes

Total RNA was extracted from C2C12 cells cultured in differentiation medium with or without Man-PEBT using the GeneJET RNA Purification Kit according to the manufacturer's instructions. The extracted total RNA was stored in GenTegra RNA tubes at room temperature. All samples demonstrated high purity, with $OD_{260/280}$ ratios between 2.1 and 2.2 as measured by a Thermo Fisher Scientific NanoDrop 2000 spectrophotometer, and exhibited excellent integrity with RNA integrity number (RIN) values of 10.0 assessed using an Agilent 5300 bioanalyzer. Stranded mRNA-seq libraries were prepared from 1 μg of total RNA using the Illumina Stranded mRNA Prep Ligation Kit following the manufacturer's protocol. The libraries were size-selected for fragments of 300−400 bp and amplified with 10−15 PCR cycles on a Bio-Rad T100 Thermal Cycler. Final library quantification was performed using a Thermo Fisher Scientific Qubit 4.0 Fluorometer, and sequencing was conducted on an Illumina NovaSeq X Plus platform (PE150) with an Illumina NovaSeq Reagent Kit. The data were analyzed on the online platform of Majorbio Cloud Platform[94,95] (see ESI for details).

Proteomes

Total protein was extracted from C2C12 cells cultured in differentiation medium with or without Man-PEBT. The extracted proteins were then digested and acidified into peptide samples using the Majorbio Microprotein Kit according to the manufacturer's instructions, followed by desalting with a C18 Tip. After drying, the peptides were reconstituted in 0.1% formic acid in water and quantified using a Thermo Fisher Scientific NanoDrop One spectrophotometer. Peptide separation was performed on a uPAC high-throughput column (75 μm × 5.5 cm) using a Vanquish Neo UHPLC system coupled to a Thermo Fisher Scientific Orbitrap Astral mass spectrometer. The mobile phase consisted of solvent A (water with 2% acetonitrile and 0.1% formic acid) and solvent B (water with 80% acetonitrile and 0.1% formic acid). Data-independent acquisition (DIA) was conducted with MS1 and MS2 mass ranges set at 380−980 m/z and 150−2000 m/z, respectively. Raw DIA data were processed using Spectronaut v19, and further analysis was conducted on the online platform of the Majorbio Cloud Platform[94,95] (see ESI for details).

Bacterial Culture and Bacterial Staining

A single bacterial colony from an agar plate was inoculated into 5 mL of liquid medium and cultured at 37 °C with shaking (170 rpm) for 12−16 h. Then, 10 μL of the resulting turbid culture was transferred into 10 mL of fresh liquid medium and incubated under the same conditions to mid-log phase. The bacteria were collected by centrifugation at 7100 rpm for 2 min, washed with PBS, and finally resuspended in PBS to an OD_{600} of 1.0 (1 OD_{600} = ∼10^9 CFU mL^{-1}). BHI medium was used for the culture of *E. faecalis*, and LB medium was used for the culture of the other strains. For bacterial staining, bacteria (1×10^8 CFU mL^{-1}) were incubated with specified concentrations of PEBT derivatives in medium at 37 °C with shaking (170 rpm) for defined periods. The bacterial suspension was either analyzed directly by flow cytometry or placed onto a glass slide, covered with a coverslip, and imaged by CLSM. For colocalization assays, bacteria (1×10^8 CFU mL^{-1}) were incubated with PEBT derivatives, washed with PBS, and then resuspended in PBS containing 10 μg/mL Hoechst 33342. The bacterial suspension was placed onto a glass slide, covered with a coverslip, and imaged by CLSM.

Antibacterial Assay

For bacterial inhibition assays, bacteria (1×10^6 CFU mL^{-1}) were incubated with specified concentrations of PEBT derivatives in LB or BHI medium at 37 °C under shaking (170 rpm) for 30 min in centrifuge tubes. The samples were then exposed to or protected from white light (20 mW cm^{-2}) for 30 min. Subsequently, the treated bacterial suspensions were transferred to a 96-well plate and further incubated at 37 °C with shaking (170 rpm) for 12 h. The OD_{600} value was measured at the absorbance of 600 nm by a microplate reader. For bacterial killing assays, bacteria (1×10^6 CFU mL^{-1}) were incubated with specified concentrations of PEBT derivatives in DMEM medium, either with or without serum, at 37 °C with shaking (170 rpm) for designated periods in centrifuge tubes. The samples were then exposed to or protected from white light (20 mW cm^{-2}) for defined periods. Subsequently, the treated bacterial suspensions were diluted 10- or 100-fold in PBS, spread on agar plates, and incubated at 37 °C for 18−24 h before colony counting. Pairwise significance markers are omitted for clarity, and comparisons are based on mean trends. A two-way ANOVA was performed with compound and concentration as factors, including their interaction, to compare the overall trends in bacterial inhibition rate between the two compound groups across the tested concentration series. ns = not significant, $^*p < 0.05$, $^{**}p < 0.01$, $^{***}p < 0.001$.

Coculture Study

For staining in the coculture system, cells were seeded in confocal dishes, and ∼80% confluence was reached for the experiment. After inoculating bacteria (1×10^8 CFU mL^{-1}) into the culture medium (without antibiotics), the coculture systems were statically cultured at 37 °C for 2 h. After rinsing off the planktonic bacteria with PBS three times, PEBT derivatives were added to the coculture system for 30 min/1 h of incubation. Then,10 μg/mL Hoechst 33342 was added before imaging by CLSM. For the antibacterial assay in the coculture system, cells were seeded in culture dishes, and ∼80% confluence was reached for the experiment. A fluidic coculture system was established, enabling direct medium exchange between two dishes via tubing connected to a peristaltic pump set at a flow rate of 0.2 mL min^{-1}. After inoculating bacteria (1×10^6 CFU mL^{-1}) into the antibiotic-free culture medium with specified concentrations of Man-PEBT, the coculture systems were statically cultured at 37 °C for 24 h. During this period, the dish without C2C12 cells was exposed to white light (20 mW cm^{-2}). while the dish with C2C12 cells was kept in the dark. Finally, the dish with C2C12 cells was observed under a microscope.

Mouse Skin Wound Infection Model

All animal experiments were conducted in accordance with the National Institutes of Health Guide for the Care and Use of Laboratory Animals and were approved by the Animal Ethics Committee of the Ethics Review Committee of Guangdong Provincial People's Hospital (Approval No.: KY2025-751-01). All procedures were performed in a biosafety level 2 facility with appropriate personal protective equipment. Efforts were made to minimize animal suffering, including the use of anesthesia for invasive procedures and the establishment of humane end points. All the mice were kept in SPF-level feeding rooms with adequate water and food. The temperature of the feeding room was kept at 26 °C, and the humidity was 50%, with a 12 h light/dark cycle. The 6-week-old mice were used to establish skin wound infection models. After administering anesthesia and performing local depilation and disinfection, a circular wound with a diameter of 10 mm was made on the back skin with the depth reaching the epidermis layer, using a puncher. After dropping 100 μL MRSA suspension (1×10^8 CFU mL^{-1}) onto the wound site three times, the infected wound was then properly sealed with protective film, and a bacterial exposure of 24 h ensured that the formation of obvious infection foci at the wound sites was observed.

In Vivo Anti-infection Evaluation

All the infected mice were randomly assigned to three groups (3 mice per group), which received the following topical treatments applied directly onto the wound surface (100 μL each) at day 0 and day 1:

Control group: PBS for 30 min, followed by exposure to white light (20 mW cm^{-2}) for 30 min.

Van group: Van (20 μg/mL) without subsequent light exposure.

Man-PEBT (Dark) group: Man-PEBT (50 μM) without subsequent light exposure.

Man-PEBT (Light) group: Man-PEBT (50 μM) for 30 min, followed by exposure to white light (20 mW cm^{-2}) for 30 min.

At day 2, wound samples were taken by swabs and thoroughly dissolved in 900 μL PBS. Subsequently, the samples were diluted 100-fold in PBS, spread on agar plates, and incubated at 37 °C for 18−24 h before colony counting. The infected wounds were monitored by macroscopic photographs once every 2 d during the wound healing process (14 d in total), and meanwhile, the body weights were measured. Pairwise comparisons of wound areas between different treatment groups on each individual day were performed using Student's t-test ($^{\#}p < 0.05$). Wound healing trends over time across treatment groups were analyzed by two-way ANOVA, considering treatment and time as factors (ns = not significant, $^{*}p < 0.05$). The mice were sacrificed after 14 d, and the tissues from wounds and major organs (heart, liver, spleen, lung, and kidney) were harvested and fixed in formalin, which were then processed into paraffin and sliced for H&E and Masson's trichrome staining analysis.

ASSOCIATED CONTENT

Supporting Information

The Supporting Information is available free of charge at https://pubs.acs.org/doi/10.1021/acsnano.6c03351.

> Syntheses and characterization details (including NMR and HRMS spectra), transcriptome and proteome analysis details, DLS measurement, additional calculation data, absorption and PL spectra, ROS generation measurement, fluorescence microscopy and flow cytometry for cells and bacteria, cytotoxicity assay, antibacterial assay, and *in vivo* experiment data (PDF)

AUTHOR INFORMATION

Corresponding Author

Xue-Wei Liu − *School of Chemistry, Chemical Engineering and Biotechnology, Nanyang Technological University, Singapore 637371, Singapore; Singapore-HUJ Alliance for Research and Enterprise (SHARE), Campus for Research Excellence and Technological Enterprise (CREATE), Singapore 138602, Singapore;* orcid.org/0000-0002-8327-6664; Email: xuewei@ntu.edu.sg

Authors

Zeyan Zhuang − *School of Chemistry, Chemical Engineering and Biotechnology, Nanyang Technological University, Singapore 637371, Singapore; Singapore-HUJ Alliance for Research and Enterprise (SHARE), Campus for Research Excellence and Technological Enterprise (CREATE), Singapore 138602, Singapore*

Yiwen Liao − *Department of Laboratory Medicine, Guangdong Provincial People's Hospital (Guangdong Academy of Medical Sciences), Southern Medical University, Guangzhou 510080, China*

Yu-Chien Lin − *School of Materials Science and Engineering, Nanyang Technological University, Singapore 639798, Singapore; Singapore-HUJ Alliance for Research and Enterprise (SHARE), Campus for Research Excellence and Technological Enterprise (CREATE), Singapore 138602, Singapore;* orcid.org/0000-0003-3290-439X

Jianqing Li − *State Key Laboratory of Luminescent Materials and Devices, Key Laboratory of Luminescence from Molecular Aggregates of Guangdong Province, South China University of Technology, Guangzhou 510640, China*

Han Ding − *School of Chemistry, Chemical Engineering and Biotechnology, Nanyang Technological University, Singapore 637371, Singapore;* orcid.org/0000-0003-3170-0723

Jiayi Hu − *School of Chemistry, Chemical Engineering and Biotechnology, Nanyang Technological University, Singapore 637371, Singapore*

Huajun Zhang − *School of Chemistry, Chemical Engineering and Biotechnology, Nanyang Technological University, Singapore 637371, Singapore;* orcid.org/0009-0002-7211-398X

Zujin Zhao − *State Key Laboratory of Luminescent Materials and Devices, Key Laboratory of Luminescence from Molecular Aggregates of Guangdong Province, South China University of Technology, Guangzhou 510640, China;* orcid.org/0000-0002-0618-6024

Ben Zhong Tang − *Guangdong Basic Research Center of Excellence for Aggregate Science, School of Science and Engineering, The Chinese University of Hong Kong (Shenzhen), Shenzhen, Guangdong 518172, China;* orcid.org/0000-0002-0293-964X

Hongwei Duan − *School of Chemistry, Chemical Engineering and Biotechnology, Nanyang Technological University, Singapore 637457, Singapore;* orcid.org/0000-0003-2841-3344

Nam-Joon Cho − *School of Materials Science and Engineering, Nanyang Technological University, Singapore 639798, Singapore; Singapore-HUJ Alliance for Research and Enterprise (SHARE), Campus for Research Excellence and Technological Enterprise (CREATE), Singapore 138602, Singapore;* orcid.org/0000-0002-8692-8955

Complete contact information is available at: https://pubs.acs.org/10.1021/acsnano.6c03351

Author Contributions

The manuscript was written through the contributions of all authors. All authors have approved the final version of the manuscript.

Notes

The authors declare no competing financial interest.

ACKNOWLEDGMENTS

We thank the Singapore National Research Foundation (CellAg, No: 370184512 and NRF-CRP31-0005), Nanyang Technological University (RG3/25), the Singapore Ministry of Health (NMRC-IRG, MOH-001738-01), the Singapore Ministry of Education (MOE-T2EP30120-0007), and the Medical Science and Technology Research Foundation of Guangdong (B2025777) for financial support.

REFERENCES

(1) Miller, W. R.; Arias, C. A. ESKAPE pathogens: Antimicrobial resistance, epidemiology, clinical impact and therapeutics. *Nat. Rev. Microbiol.* **2024**, *22*, 598−616.

(2) Ho, C. S.; Wong, C. T. H.; Aung, T. T.; Lakshminarayanan, R.; Mehta, J. S.; Rauz, S.; McNally, A.; Kintses, B.; Peacock, S. J.; de la Fuente-Nunez, C.; Hancock, R. E. W.; Ting, D. S. J. Antimicrobial resistance: A concise update. *Lancet Microbe* **2025**, *6*, 100947.

(3) Zhou, Z.; Zhou, S.; Zhang, X.; Zeng, S.; Xu, Y.; Nie, W.; Zhou, Y.; Xu, T.; Chen, P. Quaternary ammonium salts: Insights into synthesis and new directions in antibacterial applications. *Bioconjugate Chem.* **2023**, *34*, 302−325.

(4) Ibrahim, M. K.; Haria, A.; Mehta, N. V.; Degani, M. S. Antimicrobial potential of quaternary phosphonium salt compounds: A review. *Future Med. Chem.* **2023**, *15*, 2113−2141.

(5) Wang, X.; Gong, J.; Wang, J.; Zhang, F.; Mao, Z.; Liu, Z. Engineering molecular theranostic probes for antibacterial therapy. *TrAC-Trend. Anal. Chem.* **2023**, *167*, 117232.

(6) Song, Q.; Chan, S. Y.; Xiao, Z.; Zhao, R.; Zhang, Y.; Chen, X.; Liu, T.; Yan, Y.; Zhang, B.; Han, F.; Li, P. Contact-killing antibacterial mechanisms of polycationic coatings: A review. *Progr. Org. Coatings* **2024**, *188*, 108214.

(7) Zhang, J.; Guo, H.; Liu, M.; Tang, K.; Li, S.; Fang, Q.; Du, H.; Zhou, X.; Lin, X.; Yang, Y.; et al. Recent design strategies for boosting chemodynamic therapy of bacterial infections. *Exploration* **2024**, *4*, 20230087.

(8) Roque-Borda, C. A.; Primo, L. M. D. G.; Medina-Alarcón, K. P.; Campos, I. C.; Nascimento, C. D. F.; Saraiva, M. M. S.; Berchieri Junior, A.; Fusco-Almeida, A. M.; Mendes-Giannini, M. J. S.; Perdigão, J.; et al. Antimicrobial peptides: A promising alternative to conventional antimicrobials for combating polymicrobial biofilms. *Adv. Sci.* **2025**, *12* (1), 2410893.

(9) Galanakou, C.; Dhumal, D.; Peng, L. Amphiphilic dendrimers against antibiotic resistance: light at the end of the tunnel? *Biomater. Sci.* **2023**, *11*, 3379−3393.

(10) Maillard, J.-Y.; Pascoe, M. Disinfectants and antiseptics: Mechanisms of action and resistance. *Nat. Rev. Microbiol.* **2024**, *22*, 4−17.

(11) Battogtokh, G.; Choi, Y. S.; Kang, D. S.; Park, S. J.; Shim, M. S.; Huh, K. M.; Cho, Y.-Y.; Lee, J. Y.; Lee, H. S.; Kang, H. C. Mitochondria-targeting drug conjugates for cytotoxic, anti-oxidizing and sensing purposes: Current strategies and future perspectives. *Acta Pharm. Sin. B* **2018**, *8*, 862−880.

(12) Jörgensen, A. M.; Wibel, R.; Bernkop-Schnürch, A. Biodegradable cationic and ionizable cationic lipids: A roadmap for safer pharmaceutical excipients. *Small* **2023**, *19*, 2206968.

(13) Li, R.; Sun, M.; Li, Z.-H.; Qu, Y.; Li, Y.; Ampomah-Wireko, M.; Li, D.; Kong, H.; Wu, Y.; Hossain, A. A.; Zhang, E. Important role of triphenylamine in modulating the antibacterial performance relationships of antimicrobial peptide mimics by alkyl chain engineering. *J. Med. Chem.* **2025**, *68*, 10299−10313.

(14) Ismail, R.; Baaity, Z.; Cóka, I. Regulatory status quo and prospects for biosurfactants in pharmaceutical applications. *Drug Discovery Today* **2021**, *26* (8), 1929−1935.

(15) Mohapatra, S.; Yutao, L.; Goh, S. G.; Ng, C.; Luhua, Y.; Tran, N. H.; Gin, K. Y.-H. Quaternary ammonium compounds of emerging concern: Classification, occurrence, fate, toxicity and antimicrobial resistance. *J. Hazard. Mater.* **2023**, *445*, 130393.

(16) Maher, S.; Geoghegan, C.; Brayden, D. J. Safety of surfactant excipients in oral drug formulations. *Adv. Drug Delivery Rev.* **2023**, *202*, 115086.

(17) Zhou, W.; Chen, L.; Li, H.; Wu, M.; Liang, M.; Liu, Q.; Wu, W.; Jiang, X.; Zhen, X. Membrane disruption-enhanced photodynamic therapy against gram-negative bacteria by a peptide-photosensitizer conjugate. *ACS Nano* **2024**, *18*, 19771−19782.

(18) Yu, Q.; Wang, C.; Zhang, X.; Chen, H.; Wu, M. X.; Lu, M. Photochemical strategies toward precision targeting against multidrug-resistant bacterial infections. *ACS Nano* **2024**, *18*, 14085−14122.

(19) Wu, Q.; Wen, H.; Lin, W.; Sun, T.; Xie, Z. Alkyl chain engineering of boron dipyrromethenes for efficient photodynamic antibacterial treatment. *Chin. Chem. Lett.* **2024**, *35*, 109692.

(20) Li, J.; Zhuang, Z.; Dong, X.; Zhao, Z.; Tang, B. Z. Photochemical synthesis of polycyclic phosphonium salts as efficient anticancer and antibacterial agents. *Aggregate* **2025**, *6*, No. e705.

(21) Zhao, X.; Liu, J.; Fan, J.; Chao, H.; Peng, X. Recent progress in photosensitizers for overcoming the challenges of photodynamic therapy: From molecular design to application. *Chem. Soc. Rev.* **2021**, *50*, 4185−4219.

(22) Zhang, T.; Qu, X.; Shao, J.; Dong, X. Organic photosensitizers: From molecular design to phototheranostics. *Chem. Soc. Rev.* **2025**, *54*, 8406−8433.

(23) Lee, M. M. S.; Lin, D. M.; Chau, J. H. C.; Yu, E. Y.; Ding, D.; Kwok, R. T. K.; Wang, D.; Tang, B. Z. Adipocyte-targeting type I AIE photosensitizer for obesity treatment via photodynamic lipid peroxidation. *ACS Nano* **2023**, *17*, 11039−11053.

(24) Yu, J.; Xu, W.; Chen, H.; Yuan, H.; Wang, Y.; Qian, X.; Zhang, J.; Ji, Y.; Zhao, Q.; Li, S. Charge engineering of star-shaped organic photosensitizers enables efficient type-I radicals for photodynamic therapy of multidrug-resistant bacterial infection. *Adv. Healthcare Mater.* **2025**, *14* (3), 2402615.

(25) Lee, M. M. S.; Yu, E. Y.; Chau, J. H. C.; Lam, J. W. Y.; Kwok, R. T. K.; Tang, B. Z. Expanding our horizons: AIE materials in bacterial research. *Adv. Mater.* **2025**, *37* (23), 2407707.

(26) Ye, Z.; He, W.; Zhang, Z.; Qiu, Z.; Zhao, Z.; Tang, B. Z. AIEgens for microorganism-related visualization and therapy. *Interdiscip. Med.* **2023**, *1* (2), No. e20220011.

(27) Fang, Z.; Zhang, S.; Wang, W.; Xu, Y.; Lu, M.; Qian, Y.; Xiao, X.; Li, Y.; Tang, B. Z.; Zhang, M. Aggregation-induced emission-based phototheranostics to combat bacterial infection at wound sites: A review. *Biomaterials* **2025**, *315*, 122950.

(28) Zhuang, Z.; Meng, Z.; Li, J.; Shen, P.; Dai, J.; Lou, X.; Xia, F.; Tang, B. Z.; Zhao, Z. Antibacterial theranostic agents with negligible living cell invasiveness: AIE-active cationic amphiphiles regulated by alkyl chain engineering. *ACS Nano* **2022**, *16*, 11912−11930.

(29) Zheng, L.; Zhu, Y.; Sun, Y.; Xia, S.; Duan, S.; Yu, B.; Li, J.; Xu, F.-J. Flexible modulation of cellular activities with cationic photosensitizers: Insights of alkyl chain length on reactive oxygen species antimicrobial mechanisms. *Adv. Mater.* **2023**, *35* (35), 2302943.

(30) Quan, Y.-Y.; Pan, T.; Zhang, Z.; Wang, S.; Wang, G.; Yu, L.; Wang, Y.; Zang, X.-F.; Zhang, F.; Ye, X.; et al. Three-in-one: molecular engineering of D−A−π−A featured type I and type II near-infrared AIE photosensitizers for efficient photodynamic cancer therapy and bacteria killing. *Small* **2024**, *20* (46), 2402854.

(31) Zhi, M.; Sun, T.; Wang, D.; Zeng, Q.; Li, Y.; Su, X.; Feng, X.; Tang, B. Z. Regioisomeric manipulation of AIE-active photosensitizers towards multidrug-resistant bacterial eradication. *Mater. Chem. Front.* **2025**, *9*, 496−506.

(32) Wang, J.-L.; Pan, X.; Li, X.; Liu, K.-M.; Yao, M.; An, J.-Y.; Wan, Y.; Yu, X.-Q.; Feng, S.; Wu, M.-Y. Photoimmunologic therapy of stubborn biofilm via inhibiting bacteria revival and preventing reinfection. *Adv. Mater.* **2025**, *37* (6), 2411468.

(33) Mao, K.; Wang, J.; Xie, Q.; Yang, Y.-G.; Shen, S.; Sun, T.; Wang, J. Cationic nanoparticles-based approaches for immune tolerance induction in vivo. *J. Controlled Release* **2024**, *366*, 425−447.

(34) Rani, K.; Malik, A. K.; Setia, A.; Randhave, N. V.; Verma, N.; Kumar, V.; Vaishali; Deshmukh, K.; Muthu, M. S. Chitosan and its derivatives as nanotheranostics in multiple diseases management: A clinical perspective. *Carbohydr. Polym.* **2025**, *366*, 123852.

(35) Serrano-Aroca, Á.; Cano-Vicent, A.; I Serra, R. S.; El-Tanani, M.; Aljabali, A.; Tambuwala, M. M.; Mishra, Y. K. Scaffolds in the microbial resistant era: Fabrication, materials, properties and tissue engineering applications. *Mater. Today Bio.* **2022**, *16*, 100412.

(36) Patel, D. K.; Jung, E.; Priya, S.; Won, S.-Y.; Han, S. S. Recent advances in biopolymer-based hydrogels and their potential biomedical applications. *Carbohydr. Polym.* **2024**, *323*, 121408.

(37) Zhu, Y.; Zhang, X.; Chang, G.; Deng, S.; Chan, H. F. Bioactive glass in tissue regeneration: Unveiling recent advances in regenerative strategies and applications. *Adv. Mater.* **2025**, *37* (2), 2312964.

(38) Zhu, W.; Ge, M.; Liu, Q.; Yang, C.; Wang, Q.; Lin, H.; Zhang, X. Cysteine metabolism reprogramming-motivated catalytic immunotherapy for orthopedic biofilm infections. *ACS Nano* **2025**, *19*, 38894−38909.

(39) Guo, Z.; Ge, M.; Ruan, Z.; Ma, Y.; Chen, Y.; Lin, H. 2D Janus carrier-enabled trojan horse: Gallium delivery for the sequential therapy of biofilm associated infection. *Biomaterials* **2025**, *313*, 122761.

(40) Lin, Y.-C.; Ramanathan, S.; Wang, H.-Y.; Lin, Y.-C.; Liu, W.-C.; Jones, J. R.; Cho, N.-J.; Hu, C.-C.; Chung, R.-J. Engineered bioactive glass-chitosan hybrid for dual tissue and bone regeneration multifunctional healing. *Biomater Adv.* **2025**, *176*, 214340.

(41) Philips, C.; Terrie, L.; Thorrez, L. Decellularized skeletal muscle: A versatile biomaterial in tissue engineering and regenerative medicine. *Biomaterials* **2022**, *283*, 121436.

(42) Feng, L.-T.; Chen, Z.-N.; Bian, H. Skeletal muscle: Molecular structure, myogenesis, biological functions, and diseases. *MedComm* **2024**, *5*, No. e649.

(43) Jara, T. C.; Park, K.; Vahmani, P.; Eenennaam, A. L. V.; Smith, L. R.; Denicol, A. C. Stem cell-based strategies and challenges for production of cultivated meat. *Nat. Food* **2023**, *4*, 841−853.

(44) Yang, D. H.; Kook, K.-S.; Heo, Y.; Kim, W.-J. Future protein alternative: Recent progress and challenges in cellular agriculture. *Food Sci. Biotechnol.* **2025**, *34*, 423−445.

(45) Garg, K.; Brockhouse, J.; McAndrew, C. M.; Reiter, A. J.; Owens, J. G.; Mueller, R. J.; Pena, G.; Ridolfo, A.; Johnson, D. L. Regenerative rehabilitation: Navigating the gap between preclinical promises and clinical realities for treating trauma-induced volumetric muscle loss. *J. Physiol.* **2025**, *603*, 7421−7439.

(46) Xu, Y.; Zhang, H.; Liu, X.-W. Antimicrobial carbohydrate-based macromolecules: Their structures and activities. *J. Org. Chem.* **2020**, *85*, 15827−15836.

(47) Martin, H.; Lázaro, L. R.; Gunnlaugsson, T.; Scanlan, E. M. Glycosidase activated prodrugs for targeted cancer therapy. *Chem. Soc. Rev.* **2022**, *51*, 9694−9716.

(48) Maria, C.; de Matos, A. M.; Rauter, A. P. Recent antibacterial carbohydrate-based prodrugs, drugs and delivery systems to overcome antimicrobial resistance. *Curr. Opin. Chem. Biol.* **2024**, *78*, 102419.

(49) Xu, Y.; Song, S.; Duan, H.; Deng, Y.; Liu, X.-W. Combatting pathogenic bacteria with synthetic immunotherapeutics from chitosan: Antibody recruiting at engineered bacterial surface with peptidoglycan analogs. *CCS Chem.* **2024**, *6*, 1448−1457.

(50) Gu, H.; Liu, W.; Li, H.; Sun, W.; Du, J.; Fan, J.; Peng, X. 2,1,3-Benzothiadiazole derivative AIEgens for smart phototheranostics. *Coord. Chem. Rev.* **2022**, *473*, 214803.

(51) Xu, Y.; Xie, Y.; Wan, Q.; Tian, J.; Liang, J.; Zhou, J.; Song, M.; Zhou, X.; Teng, M. Mechanism research of type I reactive oxygen species conversion based on molecular and aggregate levels for tumor photodynamic therapy. *Aggregate* **2024**, *5*, No. e612.

(52) Guo, F.; Yoo, J.; Zhang, Q.; Zhao, Y.-T.; Hong, S.; Zhou, Z.-M.; Zhu, Z.-Y.; Jang, H.; Yi, C.-H.; Wang, Z.; Kim, J. S. Flexible double bonds-enhanced photodynamic therapy toward antibacterial resistance. *J. Am. Chem. Soc.* **2025**, *147*, 27932−27948.

(53) Wong, E. H. H.; Khin, M. M.; Ravikumar, V.; Si, Z.; Rice, S. A.; Chan-Park, M. B. Modulating antimicrobial activity and mammalian cell biocompatibility with glucosamine-functionalized star polymers. *Biomacromolecules* **2016**, *17*, 1170−1178.

(54) Liu, X.; Wu, M.; Wang, M.; Hu, Q.; Liu, J.; Duan, Y.; Liu, B. Direct synthesis of photosensitizable bacterial cellulose as engineered living material for skin wound repair. *Adv. Mater.* **2022**, *34* (13), 2109010.

(55) Guo, Q.; Xue, S.; Feng, J.; Peng, C.; Zhou, C.; Qiao, Y. AIE-active glycomimetics triggered bacterial agglutination and membrane-intercalating toward efficient photodynamic antiseptic. *Adv. Healthcare Mater.* **2023**, *12* (26), 2300818.

(56) Gupta, A.; Gupta, G. S. Applications of mannose-binding lectins and mannan glycoconjugates in nanomedicine. *J. Nanopart. Res.* **2022**, *24*, 228.

(57) Liu, Z.; Demontrond, F.; Imberty, A.; Sue, A. C.-H.; Vidal, S.; Zhao, H. Rim-differentiation vs. mixture of constitutional isomers: A binding study between pillar[5]arene-based glycoclusters and lectins from pathogenic bacteria. *Chin. Chem. Lett.* **2023**, *34*, 107872.

(58) Kang, B.; Okwieka, P.; Schöttler, S.; Winzen, S.; Langhanki, J.; Mohr, K.; Opatz, T.; Mailänder, V.; Landfester, K.; Wurm, F. R. Carbohydrate-based nanocarriers exhibiting specific cell targeting with minimum influence from the protein corona. *Angew. Chem., Int. Ed.* **2015**, *54*, 7436−7440.

(59) Murphy, P. V.; Bradley, H.; Tosin, M.; Pitt, N.; Fitzpatrick, G. M.; Glass, W. K. Development of carbohydrate-based scaffolds for restricted presentation of recognition groups. extension to divalent ligands and implications for the structure of dimerized receptors. *J. Org. Chem.* **2003**, *68*, 5692−5704.

(60) Xu, Y.; Zhang, Q.; Xiao, Y.; Wu, P.; Chen, W.; Song, Z.; Xiao, X.; Meng, L.; Zeng, J.; Wan, Q. Practical synthesis of latent disarmed S-2-(2-propylthio)benzyl glycosides for interrupted Pummerer reaction mediated glycosylation. *Tetrahedron Lett.* **2017**, *58*, 2381−2384.

(61) Štimac, A.; Kobe, J. Studies on the origin of stereoselectivity in the synthesis of 1,2-trans glycofuranosyl azides. *Carbohydr. Res.* **2000**, *324*, 149−160.

(62) Štimac, A.; Kobe, J. An improved preparation of 2,3,5-tri-O-acyl-*β*-D-ribofuranosyl azides by the Lewis acid-catalysed reaction of *β*-D-ribofuranosyl acetates and trimethylsilyl azide: An example of concomitant formation of the *α* anomer by trimethylsilyl triflate catalysis Carbohydr. *Res* **1992**, *232*, 359−365.

(63) Zhuang, Z.; Dai, J.; Yu, M.; Li, J.; Shen, P.; Hu, R.; Lou, X.; Zhao, Z.; Tang, B. Z. Type I photosensitizers based on phosphindole oxide for photodynamic therapy: Apoptosis and autophagy induced by endoplasmic reticulum stress. *Chem. Sci.* **2020**, *11*, 3405−3417.

(64) Li, J.; Zhuang, Z.; Zhao, Z.; Tang, B. Z. Type I AIE photosensitizers: Mechanism and application. *VIEW* **2022**, *3*, 20200121.

(65) Setsukinai, K.; Urano, Y.; Kakinuma, K.; Majima, H. J.; Nagano, T. Development of novel fluorescence probes that can reliably detect reactive oxygen species and distinguish specific species. *J. Biol. Chem.* **2003**, *278*, 3170.

(66) Entradas, T.; Waldron, S.; Volk, M. The detection sensitivity of commonly used singlet oxygen probes in aqueous environments. *J. Photochem. Photobiol., B* **2020**, *204*, 111787.

(67) Liu, S.; Wang, B.; Yu, Y.; Liu, Y.; Zhuang, Z.; Zhao, Z.; Feng, G.; Qin, A.; Tang, B. Z. Cationization-enhanced type I and type II ROS generation for photodynamic treatment of drug-resistant bacteria. *ACS Nano* **2022**, *16*, 9130.

(68) Wang, Y.; Liao, J.; Lyu, Y.; Guo, Q.; Zhu, Z.; Wu, X.; Yu, J.; Wang, Q.; Zhu, W.-H. An AIE photosensitizer with simultaneous type I and type II ROS Generation: Efficient bacterial elimination and hypoxic tumor ablation. *Adv. Funct. Mater.* **2023**, 33 (33), 2301692.

(69) Fu, X.; Zhuang, C.-I.; Hu; Hu, P. P Regulation of muscle stem cell fate. *Cell Regen* **2022**, *11* (1), 40.

(70) Yi, T.; Huang, S.; Liu, G.; Li, T.; Kang, Y.; Luo, Y.; Wu, J. Bioreactor synergy with 3D scaffolds: New era for stem cells culture. *ACS Appl. Bio Mater.* **2018**, *1*, 193−209.

(71) Ahmad, K.; Shaikh, S.; Chun, H. J.; Ali, S.; Lim, J. H.; Ahmad, S. S.; Lee, E. J.; Choi, I. Extracellular matrix: The critical contributor to skeletal muscle regeneration—a comprehensive review. *Inflammation Regener* **2023**, *43*, 58.

(72) Desai, N.; Sahel, D.; Kubal, B.; Postwala, H.; Shah, Y.; Chavda, V. P.; Fernandes, C.; Khatri, D. K.; Vora, L. K. Role of the extracellular matrix in cancer: insights into tumor progression and therapy. *Adv. Therap* **2025**, *8* (2), 2400370.

(73) Hwang, M.; Lee, E.-J.; Chung, M.-J.; Park, S. Y.; Jeong, K.-S. Five transcriptional factors reprogram fibroblast into myogenic lineage cells via paraxial mesoderm stage. *Cell Cycle* **2020**, *19*, 1804−1816.

(74) Scala, P.; Lovecchio, J.; Lamparelli, E. P.; Vitolo, R.; Giudice, V.; Giordano, E.; Selleri, C.; Rehak, L.; Maffulli, N.; Della Porta, G. Myogenic commitment of human stem cells by myoblasts co-culture: A static vs. a dynamic approach. *Artif. Cells, Nanomed., Biotechnol.* **2022**, *50*, 49−58.

(75) Guan, X.; Yan, Q.; Ma, Z.; Zhou, J. Production of mature myotubes in vitro improves the texture and protein quality of cultured pork. *Food Funct.* **2023**, *14*, 3576−3587.

(76) Eigler, T.; Zarfati, G.; Amzallag, E.; Sinha, S.; Segev, N.; Zabary, Y.; Zaritsky, A.; Shakked, A.; Umansky, K.-B.; Schejter, E. D.; Millay, D. P.; Tzahor, E.; Avinoam, O. ERK1/2 inhibition promotes robust myotube growth via CaMKII activation resulting in myoblast-to-myotube fusion. *Dev. Cell* **2021**, *56*, 3349−3363.

(77) Daley, W. P.; Yamada, K. M. ECM-modulated cellular dynamics as a driving force for tissue morphogenesis. *Curr. Opin. Genet. Dev.* **2013**, *23*, 408−414.

(78) Blache, U.; Stevens, M. M.; Gentleman, E. Harnessing the secreted extracellular matrix to engineer tissues. *Nat. Biomed. Eng.* **2020**, *4*, 357−363.

(79) Braun, T.; Gautel, M. Transcriptional mechanisms regulating skeletal muscle differentiation, growth and homeostasis. *Nat. Rev. Mol. Cell Biol.* **2011**, *12*, 349−361.

(80) Kim, J. W.; Bae, J.-H.; Go, G.-Y.; Lee, J.-R.; Jeong, Y.; Kim, J.-Y.; Kim, T. H.; Kim, Y. K.; Han, J.-W.; Oh, J.-E.; Hahn, M.-J.; Kang, J.-S.; Bae, G.-U. Epsti1 regulates the inflammatory stage of early muscle regeneration through STAT1-VCP interaction. *Int. J. Biol. Sci.* **2024**, *20*, 3530−3543.

(81) Sharma, A.; Zehra, A.; Mathew, S. J. Myosin heavy chain-perinatal regulates skeletal muscle differentiation, oxidative phenotype and regeneration. *FEBS J.* **2024**, *291*, 2836−2848.

(82) Melzener, L.; Schaeken, L.; Fros, M.; Messmer, T.; Raina, D.; Kiessling, A.; Haaften, T.; Spaans, S.; Doğan, A.; Post, M. J.; et al. Optimisation of cell fate determination for cultivated muscle differentiation. *Commun. Biol.* **2024**, *7*, 1493.

(83) Thomas, K.; Engler, A. J.; Meyer, G. A. Extracellular matrix regulation in the muscle satellite cell niche. *Connect. Tissue Res.* **2015**, *56*, 1−8.

(84) Taylor, L.; Wankell, M.; Saxena, P.; McFarlane, C.; Hebbard, L. Cell adhesion an important determinant of myogenesis and satellite cell activity. *BBA-Mol. Cell Res.* **2022**, *1869*, 119170.

(85) Santos, M. D.; Backer, S.; Auradé, F.; Wong, M. M.-K.; Wurmser, M.; Pierre, R.; Langa, F.; Cruzeiro, M. D.; Schmitt, A.; Concordet, J.-P.; et al. A fast Myosin super enhancer dictates muscle fiber phenotype through competitive interactions with Myosin genes. *Nat. Commun.* **2022**, *13* (1), 1039.

(86) Schiaffino, S. Muscle fiber type diversity revealed by anti-myosin heavy chain antibodies. *FEBS J.* **2018**, *285*, 3688−3694.

(87) Parker, M. F. L.; Flavell, R. R.; Luu, J. M.; Rosenberg, O. S.; Ohliger, M. A.; Wilson, D. M. Small molecule sensors targeting the bacterial cell wall. *ACS Infect. Dis.* **2020**, *6*, 1587−1598.

(88) You, Y.; Yu, X.; Jiang, J.; Chen, Z.; Zhu, Y.-X.; Chen, Y.; Lin, H.; Shi, J. Bacterial cell wall-specific nanomedicine for the elimination of Staphylococcus aureus and Pseudomonas aeruginosa through electron-mechanical intervention. *Nat. Commun.* **2025**, *16*, 2836.

(89) Lu, T.*Sobtop, Version 1.0]*, http://sobereva.com/soft/Sobtop (Accessed on 20th February 2026).

(90) Lu, T. A comprehensive electron wavefunction analysis toolbox for chemists. Multiwfn. *J. Comput. Chem.* **2024**, *161*, 082503.

(91) Zhang, J.; Lu, T. Efficient evaluation of electrostatic potential with computerized optimized code. *Phys. Chem. Chem. Phys.* **2021**, *23*, 20323−20328.

(92) Niu, Y.; Li, W.; Peng, Q.; Geng, H.; Yi, Y.; Wang, L.; Nan, G.; Wang, D.; Shuai, Z. MOlecular MAterials Property Prediction Package (MOMAP) 1.0: A software package for predicting the luminescent properties and mobility of organic functional materials. *Mol. Phys.* **2018**, *116*, 1078−1090.

(93) Neese, F. Software update: The ORCA program system—Version 5.0. *Wiley Interdiscip. Rev.: comput. Mol. Sci.* **2022**, *12*, No. e1606.

(94) Han, C.; Shi, C.; Liu, L.; Han, J.; Yang, Q.; Wang, Y.; Li, X.; Fu, W.; Gao, H.; Huang, H.; et al. Majorbio Cloud 2024: Update single-cell and multiomics workflows. *iMeta* **2024**, *3*, No. e217.

(95) Majorbio Cloud Platform *Majorbio Cloud Platform*. https://cloud.majorbio.com (Accessed on 20th February 2026).